ELEMENTA
Science of the Anthropocene

Thielke, L, et al. 2024. Spatio-temporal variability of small-scale leads based on helicopter maps of winter sea ice surface temperatures. *Elem Sci Anth*, 12: 1. DOI: https://doi.org/10.1525/elementa.2023.00023

RESEARCH ARTICLE

Spatio-temporal variability of small-scale leads based on helicopter maps of winter sea ice surface temperatures

Linda Thielke[1], Gunnar Spreen[1,*], Marcus Huntemann[1], and Dmitrii Murashkin[1,2]

Observations of sea ice surface temperature provide crucial information for studying Arctic climate, particularly during winter. We examined 1 m resolution surface temperature maps from 35 helicopter flights between October 2, 2019, and April 23, 2020, recorded during the Multidisciplinary drifting Observatory for the Study of Arctic Climate (MOSAiC). The seasonal cycle of the average surface temperature spanned from 265.6 K on October 2, 2019, to 231.8 K on January 28, 2020. The surface temperature was affected by atmospheric changes and varied across scales. Leads in sea ice (cracks of open water) were of particular interest because they allow greater heat exchange between ocean and atmosphere than thick, snow-covered ice. Leads were classified by a temperature threshold. The lead area fraction varied between 0% and 4% with higher variability on the local (5–10 km) than regional scale (20–40 km). On the regional scale, it remained stable at 0–1% until mid-January, increasing afterward to 4%. Variability in the lead area is caused by sea ice dynamics (opening and closing of leads), as well as thermodynamics with ice growth (lead closing). We identified lead orientation distributions, which varied between different flights but mostly showed one prominent orientation peak. The lead width distribution followed a power law with a negative exponent of 2.63, which is in the range of exponents identified in other studies, demonstrating the comparability to other data sets and extending the existing power law relationship to smaller scales down to 3 m. The appearance of many more narrow leads than wide leads is important, as narrow leads are not resolved by current thermal infrared satellite observations. Such small-scale lead statistics are essential for Arctic climate investigations because the ocean–atmosphere heat exchange does not scale linearly with lead width and is larger for narrower leads.

Keywords: Arctic, Sea ice, Leads, Surface temperature, Helicopter, MOSAiC

1. Introduction

The investigation of sea ice processes is crucial for studying climate warming, which is especially strong at high northern latitudes where it is called Arctic Amplification (Serreze and Barry, 2011; Wendisch et al., 2017; Dai et al., 2019; Intergovernmental Panel on Climate Change [IPCC], 2021). Sea ice becomes significantly thinner (Meredith et al., 2019; IPCC, 2021), with an average reduction of 2 m, from the period 1958–1976 (submarine record) to the current altimeter period, with strongest thinning during 2003–2008 (the ICESat period; Kwok, 2018). With the decline in annual sea ice minimum extent in late summer, the multiyear ice area has also decreased strongly (Kwok, 2018). Thinner sea ice makes the ice more susceptible to wind and ocean current forcing, resulting in higher ice drift speeds (Spreen et al., 2011; Kwok et al., 2013). Rampal et al. (2009) hypothesized that thinner sea ice has less mechanical strength, allowing easier breaking of the ice. The changing sea ice conditions influence the heat exchange between ocean and atmosphere, which is important for the whole Earth Climate System and not only the Arctic regions (Serreze et al., 2009; Meredith et al., 2019). A better understanding of the interaction between ocean, sea ice, and atmosphere is essential.

This study presents the spatio-temporal evolution of the Arctic sea ice surface temperature and lead area fraction, as well as the lead width and orientation angle for the Multidisciplinary drifting Observatory for the Study of Arctic Climate (MOSAiC), i.e., its Central Observatory (CO) and surroundings (Shupe et al., 2020). We refer to all fractures in the sea ice cover as leads, while fractures are usually referred to as leads only if their widths are >50 m (World Meteorological Organization, 2014). The MOSAiC expedition (September 2019–October 2020) allowed us to collect in-situ measurements from the central Arctic over a whole seasonal cycle for various aspects of the Arctic system (Nicolaus et al., 2022; Rabe et al., 2022; Shupe et al., 2022) following the same ice along the Transpolar

[1] Institute of Environmental Physics, University of Bremen, Bremen, Germany

[2] German Aerospace Center (DLR), Remote Sensing Technology Institute (IMF), Bremen, Germany

* Corresponding author:
Email: gunnar.spreen@uni-bremen.de

drift. The analysis is based on thermal infrared (TIR) helicopter-borne surface temperature measurements during 35 helicopter survey flights between October 2019 and April 2020. Our measurement program was part of the sea ice and remote sensing teams, whose efforts generated extensive datasets on sea ice physics, including albedo, ice and snow properties, as well as microwave and optical properties of sea ice (Nicolaus et al., 2022). Such an extensive collection of observations in the central Arctic had not been obtained before. With this study we provide a detailed description of the results from the helicopter-borne surface temperature maps and the derived lead properties, and compare them to previous work. We address three main points: the seasonal evolution of winter surface temperatures and scale-dependent spatial variability; the difference in lead fraction evolution on local and regional scales and possible explanations; and whether the distribution of lead width follows a power law with an exponent similar to literature values, down to a lead width of 3 m.

Our measurements with helicopter-borne TIR imaging provide temperatures of the sea ice surface with a high spatial resolution of 1 m. This resolution is substantially higher than that of TIR satellite sensors, like the Moderate Resolution Imaging Spectroradiometers (MODIS), which have a grid resolution of 1 km (the actual spatial resolution increases to 4.8 $\times$ 2.4 km for high incidence angles; Masuoka et al., 1998). Nevertheless, satellites are the primary tool for observing the Arctic sea ice state (Spreen and Kern, 2017; Fox-Kemper et al., 2021). Compared to the pan-Arctic coverage from satellites, we provide with our helicopter data a restricted areal coverage from a local 5 km scale to a regional 40 km scale. Investigating the small-scale variability is important to better understand the representation of sea ice properties in models and satellite retrievals on a subgrid scale (Vihma et al., 2014). Thus, our high spatial resolution data is valuable for evaluating models and satellite retrievals (Ivanova et al., 2016).

Open water and thin ice areas influence the Arctic heat budget by allowing increased heat exchange between the ocean and the atmosphere. The TIR temperatures distinguish open water and thin ice from thick ice, particularly for a thin ice thickness of less than 1 m (Shokr and Sinha, 2015). Above a 1 m ice thickness, changes in the heat flux between ocean and atmosphere are minimal and have minor relevance for the Arctic heat budget (Maykut, 1982). Open water rarely exists in winter because the freezing starts directly after a lead opens. Therefore, we expect to capture mainly thin ice and only small open-water areas with significantly warmer surface temperatures.

During winter, the heat loss is more than an order of magnitude larger in leads compared to the surrounding ice (Maykut, 1982). Leads have a high variability in time and space (Yu and Rothrock, 1996; Willmes and Heinemann, 2015). Therefore, monitoring their characteristics throughout the year is important. In Arctic pack ice during winter, a lead area fraction (open water and thin ice combined) of less than 10% is expected (Yu and Rothrock, 1996). Maykut (1982) found that in winter, the heat contribution from thin ice in leads is similar to the open water areas and larger than from the dominating thick ice area. Willmes and Heinemann (2016), using MODIS for the period 2003–2015, and Wang et al. (2016), using the Finite Element Sea Ice-Ocean Model (FESOM) for the period 1985–2014, did not find a trend in the lead area fraction evolution. Additionally, Wang et al. (2016) found that the winds mainly determine the inter-annual variability in lead area fraction. However, a precise determination of the lead area fraction is crucial. Lüpkes et al. (2008) showed that a slight change in the high sea ice concentration (SIC) range, e.g., by the opening of leads, affects the near-surface air temperature. According to their study, a change of 1% in SIC could cause an air temperature change of up to 3.5 K. Small reductions in SIC, mostly induced by leads, allow a stronger (non-linear) heat exchange between the ocean and atmosphere than when a closed sea ice cover is present (Maykut, 1978). Esau (2007) and Marcq and Weiss (2012) demonstrated the importance of narrow leads for the heat exchange. Monitor changes in winter lead area fraction and associated changes in sea ice concentration is therefore necessary.

We first describe the helicopter measurement program and surface temperature maps, which are the key datasets for this study, along with the supporting data. We further explain the methods of lead classification and segmentation. We then present the results in three parts. First, we analyze the temporal variability of the surface temperature on different spatial scales. Second, we present the spatio-temporal variability of the lead area fraction and a case study of the November 2019 storm event. Third, we focus on the lead properties, i.e., width and orientation. We conclude with a discussion of the presented results, as well as a summary and outlook.

2. Data and methods

This section presents the data used in this study: first, the surface temperature maps; and, second, the supporting atmospheric data. Further, the methods for lead classification and lead segmentation are explained.

2.1. Surface temperature maps

The surface temperature maps in this study are based on helicopter-borne TIR imaging (Thielke et al., 2022b). With an infrared camera (InfraTec VarioCAM HD) installed, 35 helicopter flights were performed on a roughly weekly basis between October 2, 2019, and April 23, 2020, from RV *Polarstern* (Alfred-Wegener-Institut Helmholtz-Zentrum für Polar- und Meeresforschung, 2017; **Figure 1**). The set of flights consists of four main flight patterns: (i) Central Observatory (local), (ii) L-Site triangles (regional), (iii) L-Site grids, and (iv) event-related, like the mapping of particular leads. Details about the surface temperature maps (Thielke et al., 2022a) and pre-processing are presented in Thielke et al. (2022b). The main processing steps to obtain the TIR maps from the single images included correction of artefacts in images, georeferencing, ice drift correction and correction of temporal temperature changes within one flight. To our knowledge, regional scale sea ice infrared imaging has not been analyzed and published before, as now presented in this study. Unprocessed data from nine more flights are available (Thielke et al., 2022b).

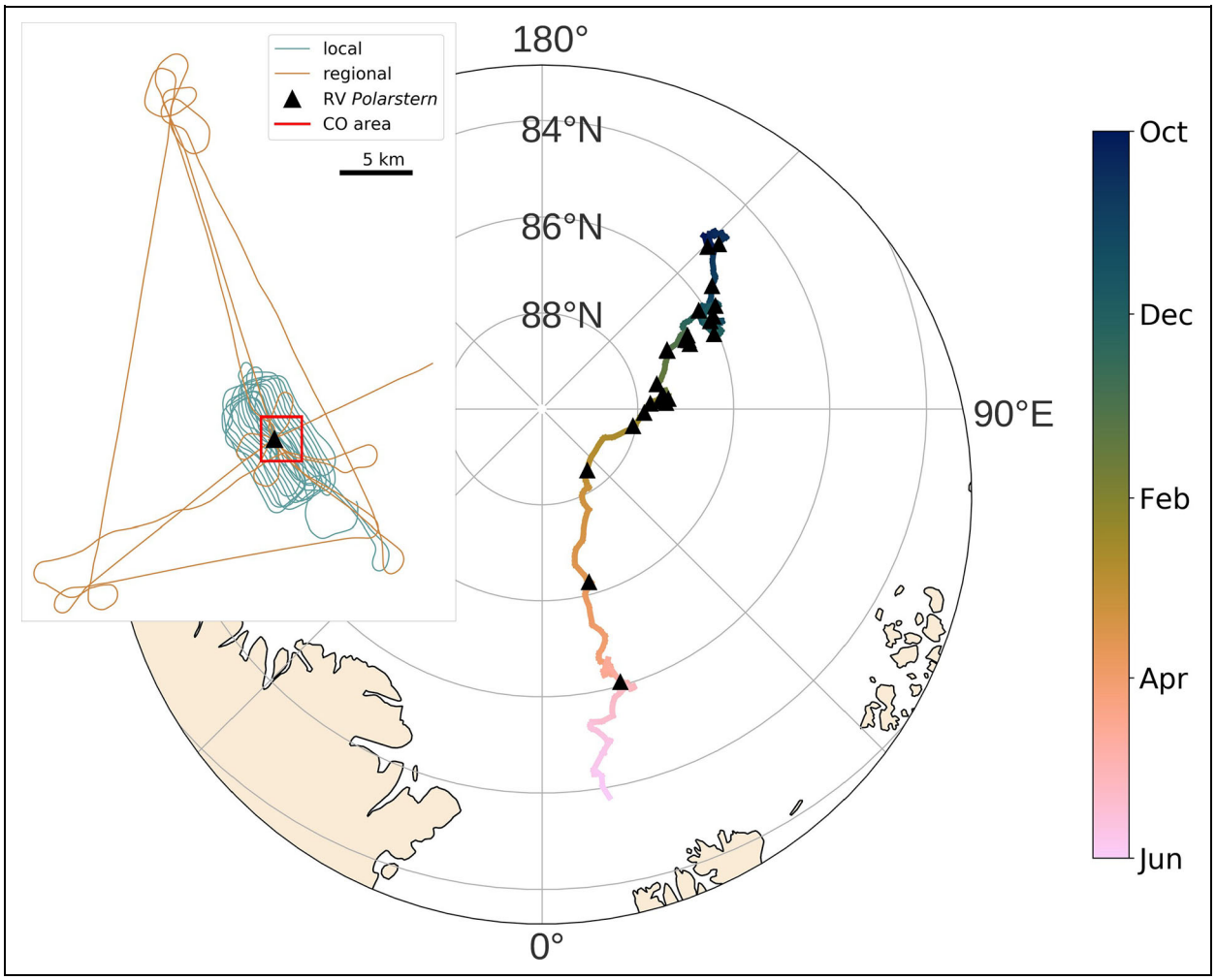

Figure 1. Helicopter flight locations and flight patterns. The colored track shows the drift of RV *Polarstern* from October 2019 until June 2020. The black triangles represent the location of the 35 helicopter flights. Additionally, as inlay on the left, we show a typical local (turquoise) and regional (orange) flight pattern with *Polarstern* as the center (black triangle). The red box marks the Central Observatory (CO) area (see Figure S3 in the supplemental material for more information on the CO).

The radiation in the TIR spectral region has a very small penetration depth on the sub-millimeter scale in snow and ice (see pages 272 and 294 in Shokr and Sinha, 2015). As a result, the TIR brightness temperature provides a measurement of the upper surface of snow or sea ice. Thus, the recorded temperature is expected to be influenced by atmospheric changes through the radiation balance at the snow/ice-air interface. Clouds strongly influence the surface temperature (Vihma and Pirazzini, 2005) by reducing the radiative cooling (Wang et al., 2001). Our flights were performed only during calm and clear weather conditions. Thus, we could neglect a dependence on changing cloud cover. However, the changing air temperature still plays a role, which needs to be taken into account (Thielke et al., 2022b).

2.2. Supporting atmospheric data

We used atmospheric data from the 10 m meteorological mast on the MOSAiC ice floe: 2 m air temperature, measured with a Vaisala HMT 330; 10 m wind direction; and 10 m wind speed, measured with a Metek uSonic-3 cage (Cox et al., 2021). These supporting measurements were made at the location of Met City in the CO. Details are presented in Shupe et al. (2022).

2.3. Lead classification

Leads were classified based on a temperature threshold applied to the surface temperature maps. We applied a binary classification, discriminating between snow-covered thick sea ice (cold regime) and leads (warm regime), which are mostly covered with thin ice due to the fast freezing of the ocean surface under cold winter conditions. We used the "time-fixed surface temperature" to avoid the influence of changes in surface temperature during one flight. The thermal distinction for surface types with larger ice thickness becomes weaker due to low heat transfer through the ice (Maykut, 1978). Thus, the discrimination of leads from thick ice is easier due to large temperature differences; we do not aim to discriminate the thick ice classes further (e.g., between first-year and second-year ice). We applied the iterative threshold selection from Ridler and Calvard (1978) to the two-dimensional surface temperature arrays. A detailed description is provided in the

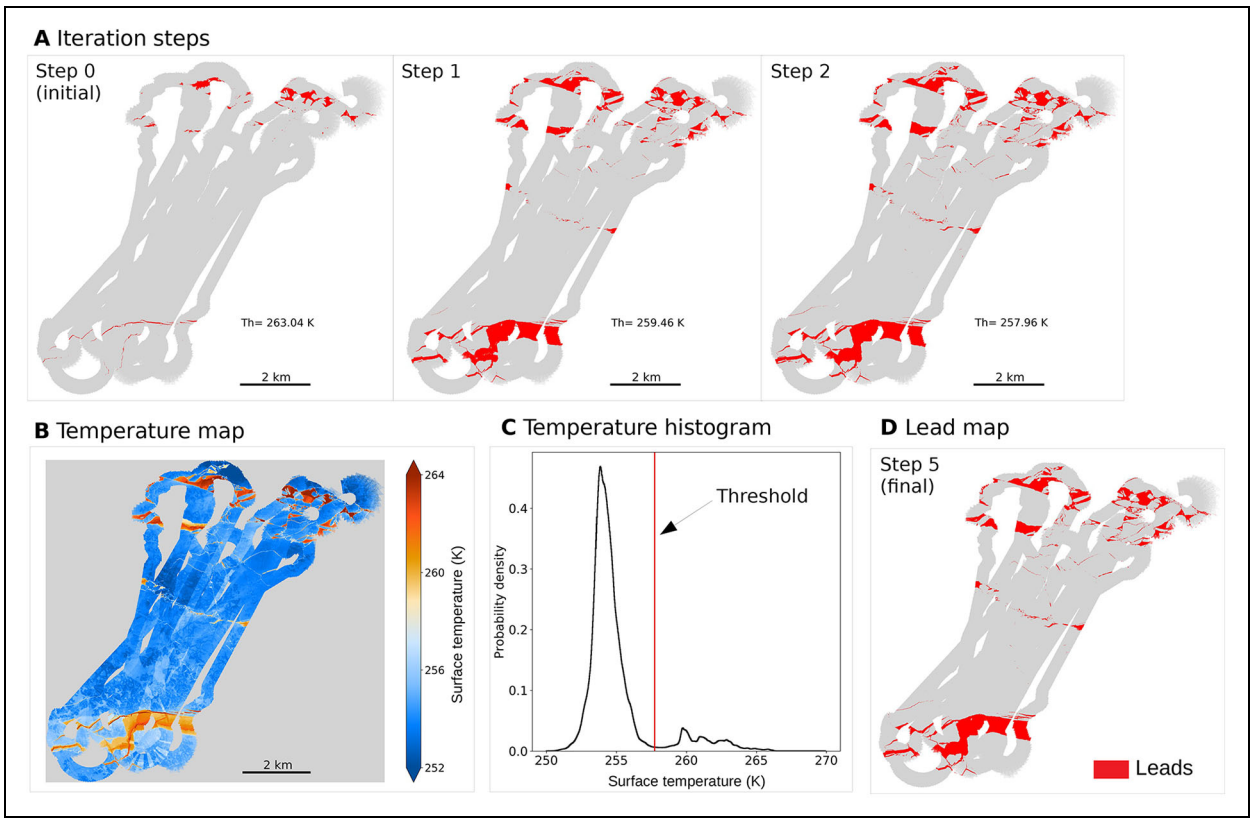

Figure 2. Lead classification example for the flight on October 20, 2019. (A) Results from steps 0, 1, and 2 for the iterative threshold selection; (B) the gridded surface temperature maps; (C) the temperature distribution of (B); and (D) final (step 5) binary lead classification based on data in (B). The red vertical line in (C) represents the iterative temperature threshold found to discriminate between lead surfaces (red area) and no lead surfaces (gray areas; in (A) and (D))

supplemental material Text S1, Figure S1, and Table S1. We worked with dynamic thresholds for different flights in order to establish the same classes defined with different surface temperature distributions in different flights. The dynamic threshold is required because the surface temperature is strongly connected to the ambient air temperature, which varies with time (Section 3.2).

2.3.1. Classification example from October 20, 2019

The threshold-based lead classification is exemplified by the flight on October 20, 2019, at the beginning of the winter season (**Figure 2**). We show steps 0 (initial threshold) to 2 for the temperature threshold iteration (**Figure 2A**). With step 2, the result is already close to the final result (step 5) shown in **Figure 2D**. The surface temperature (**Figure 2B**) is dominated by low temperatures (blue) associated with snow-covered thick ice; the warm surface temperatures (red) are referred to as leads. The binary classification map (**Figure 2D**) resulting in sea ice (gray) or leads (red) is based on the iterative temperature threshold applied to the temperature distribution (**Figure 2C**), showing the two classes as two main temperature regimes. The lead area fraction for this case on October 20 is the highest in our time series, with close to 10% for the full area covered by the helicopter flight.

2.4. Lead segmentation

We applied a segmentation algorithm to the lead map to define the properties of single leads, i.e, width and orientation. The segmentation was performed according to the watershed segmentation (Najman and Schmitt, 1994). Next, a set of object lead properties, i.e., width and orientation from enclosing ellipse, its area, orientation, and major axis, were derived based on Burger and Burge (2009) with "scikit-image" library for Python.

In **Figure 3**, we illustrate the object properties for two example lead segments. The warmer temperatures on the left (yellow) are classified as lead, consistent with the red areas on the right that indicate the lead areas. We retrieved the lead properties of width and orientation (calculated from ellipse parameters), assuming that they are representative, even if the ellipse does not cover the full lead due to the limited spatial coverage of our data or if the lead is interrupted. We therefore only determined width but not length of the leads. The key lead parameters are the classified area (red) in the enclosing rectangle (dashed line in **Figure 3**), the minor and major axes, and the orientation of the ellipse (pointing in the direction of the major axis). The zero line for the orientation is the north–south axis (all our surface temperature maps are oriented North along the y-axis). The ellipse defined for the lead segment is not representing the real length, but is considered a stable approximation for an object of arbitrary shape. Generally, the ellipses of close-by leads can overlap, which is required to calculate the lead properties individually, even though the two lead segments are not overlapping (Figure S2 in the supplemental material).

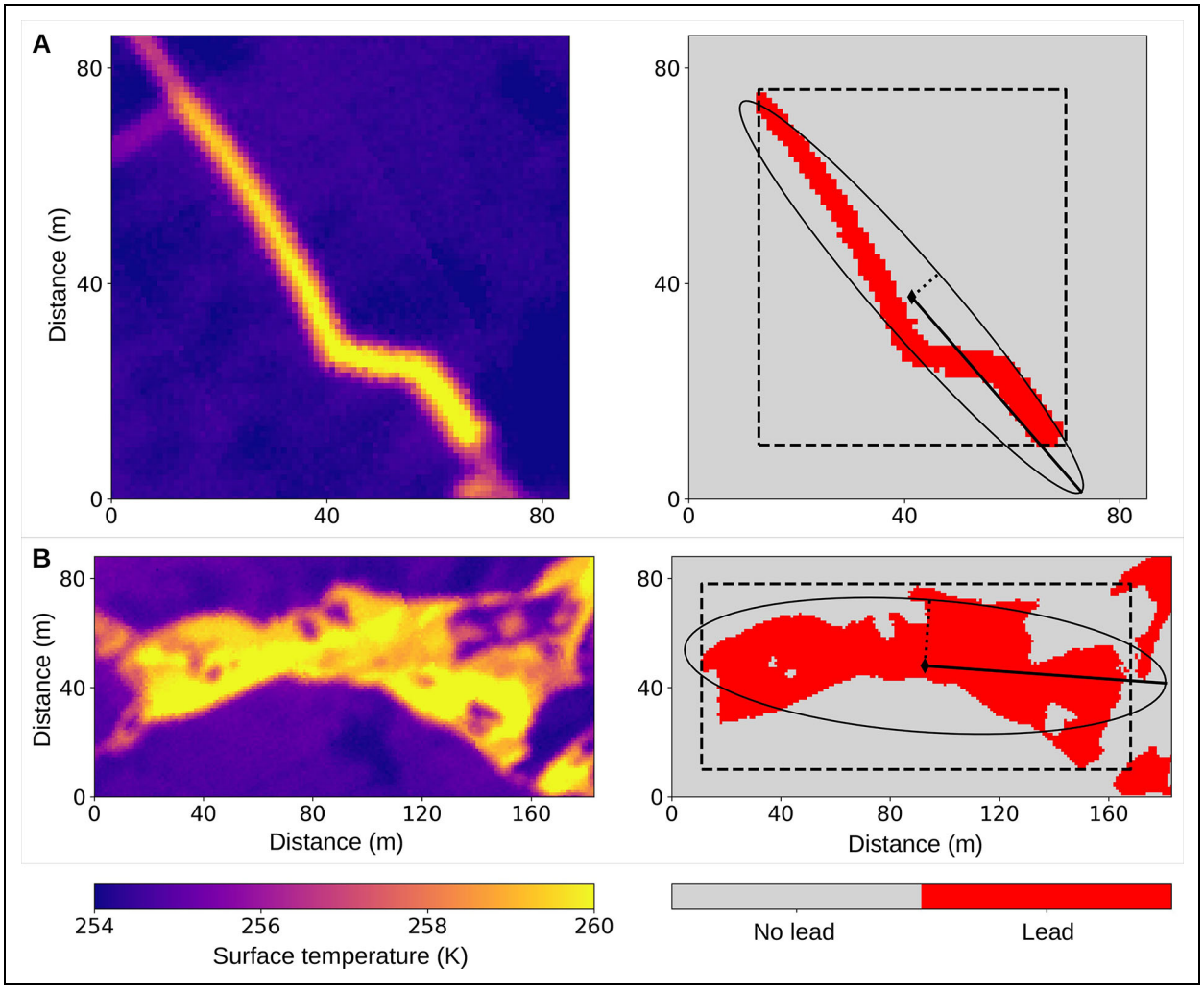

Figure 3. Lead segmentation to derive lead width and orientation properties. Two lead segments from the lead classification result of the flight on October 20, 2019, with the temperature map on the left and the lead classification including the ellipse geometry on the right. The major axis (solid) and minor axis (dotted) of each ellipse are shown. The dashed rectangle marks the area from which the classified area in red was determined. (A) A narrow lead with mean width of 3 m and orientation (of the major axis) of −41°. (B) A wider and slightly scattered lead with mean width of 26 m and orientation of −86°.

We had to account for some artificial effects, such as the map's edge or shifts inside the map caused by small offsets in the geolocation of different helicopter overflights. Shifts or gaps could cause an artificial break of a lead into more segments, when it was only a single lead in situ. Also, due to changes in ice drift direction (e.g., shear), which can cause real breaks and gaps in the classified leads, the segments can represent a subset of a lead. The segments of the subsets of leads will result in an overestimation of the total number of leads. However, such an overestimate is not expected to impact our results for lead width and orientation (we do not analyze the number of leads). Therefore, we assume the segmentation is representative for the purpose of an overall statistical analysis of lead width and orientation.

3. Winter surface temperatures

Based on the series of 35 helicopter flights with the TIR camera during the MOSAiC winter, we present and discuss the spatio-temporal variability of the winter surface temperatures recorded during MOSAiC. In this study we used the gridded time-fixed helicopter surface temperature maps (Thielke et al., 2022a, 2022b), which will be referred to as surface temperature for simplicity. First, we provide the meteorological context for the MOSAiC winter, which supports the explanation of the results. Then, we present the complete seasonal cycle of the surface temperature across the MOSAiC CO and its surrounding for the whole winter 2019/2020. Afterward, we show the spatial temperature variability within the surface temperature maps.

3.1. Meteorological context

How representative are our results from the MOSAiC winter in terms of surface temperature (this section) and lead area fraction (Section 4) in context with the meteorological condition? The meteorological conditions are discussed in Rinke et al. (2021) based on the ERA5

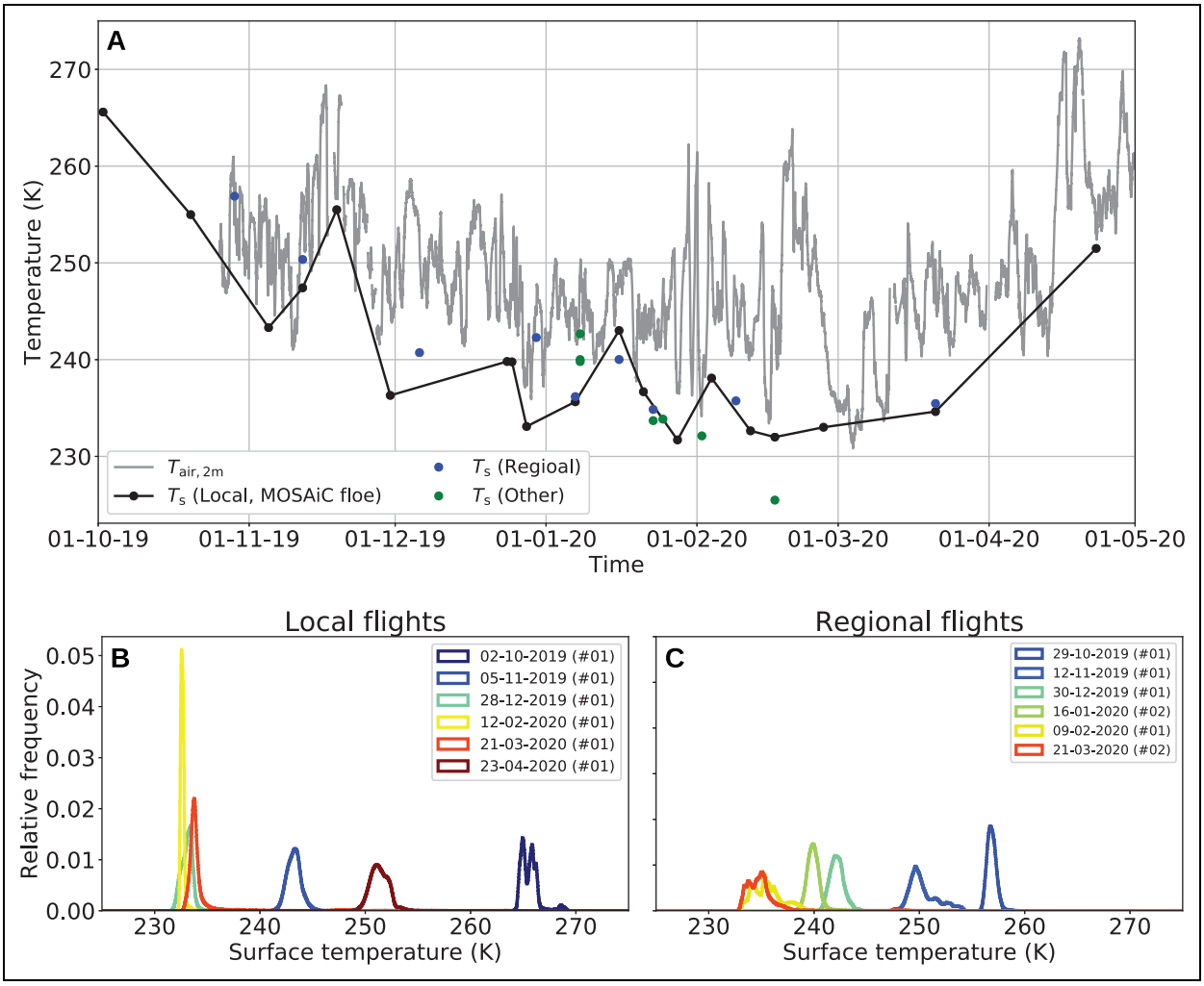

Figure 4. Evolution of MOSAiC surface temperatures from 35 helicopter flights. (A) Temporal evolution of the average surface temperature of each flight throughout winter 2019/2020 from October 2, 2019, to April 23, 2020. Black indicates the local flights covering the Central Observatory. They are connected to show the temporal evolution of the primary MOSAiC observation area. The regional flights, repeatedly visiting the L-Sites in the MOSAiC distributed network, are displayed in blue, whereas green shows additional flights not falling in one of these two categories. The gray line represents the 2 m air temperature measured at the floe in Met City (location for meteorological measurements within the Central Observatory). In the lower panel, a selection of surface temperature distributions is shown for different dates in the winter for (B) the local and (C) the regional flights. The colors continue from blue (begin of the winter) to red (end of the winter).

reanalysis data between 1979 and 2019; they were mostly typical during MOSAiC, although some unusual events happened before the expedition and during our observation period. Summer 2019, before the MOSAiC expedition started, was very warm with unusually long low sea ice extent as well as thinner ice (Krumpen et al., 2020; Rinke et al., 2021). During the expedition, unusual conditions occurred during the following periods, all according to Rinke et al. (2021):

- unusual cold at the beginning of November 2019 and March 2020;
- warming events in mid-November, beginning of December, mid-February, and mid-April;
- unusual positive Arctic Oscillation with associated fast sea ice drift in spring 2020 (Krumpen et al., 2021; Dethloff et al., 2022);
- anomalous low pressure January to April 2020 associated with more frequent storm events during winter and spring (relatively low cyclone counts for October 2019 to January 2020).

3.2. Surface temperature evolution

The surface temperature of sea ice varied on short timescales, i.e., within the flight duration of 90 min. This effect, however, was largely corrected in the surface temperature maps. Please see Thielke et al. (2022b) for how corrected and time-fixed surface temperature maps are calculated. Here, we discuss the seasonal variability of surface temperature. The average surface temperature per flight decreased from October 2, 2019, at 265.6 K until reaching its minimum at 231.8 K on January 28, 2020 (**Figure 4A**). Later in the winter season, the average

surface temperature increased to 251.4 K until the last flight on April 23, 2020, when at that time, the 2 m air temperature was already about 20 K higher and close to the freezing point.

The temporal evolution of the surface temperature was comparable to that of the 2 m air temperature. This comparability is consistent with our expectation that, due to the shallow penetration depth (micrometer range) of electromagnetic waves in the TIR region (Section 2.1), air temperature will have a substantial influence on our surface temperature observations. Also, Vihma and Pirazzini (2005) highlighted the importance of the surface temperature and coupling to the atmosphere. At the same time, the heterogeneity of the surface temperature in ice-covered regions can also influence the atmosphere. But as long as the surface is frozen, the surface temperatures stay well below the freezing point. Generally, the surface temperature can be cooler than the air temperature during clear sky conditions due to radiative cooling.

A prominent interruption in the cooling happened at the beginning of the winter in mid-November due to a substantial increase in the surface and air temperature caused by a storm event (Rinke et al., 2021). More warming events (Section 3.1) are reflected in the surface temperature record. From mid-February onward, the frequency of flights was reduced, so we cannot reflect all single atmospheric events. However, we can show the warming of the surface temperature toward spring.

3.3. Spatial temperature variability

The spread of the surface temperature varied from flight to flight. A wider distribution indicates the presence of several ice classes and spreads toward warmer temperatures. This variability is illustrated with the selection of six exemplary surface temperature distributions, each for local and regional scales, throughout the winter season (**Figure 4B** and **C**). The major peak represents the predominant surface type, snow-covered thick ice, in all cases. The surface temperatures of this thick ice are more similar to the 2 m air temperature because of the reduced heat flux from the ocean through the insulating thick ice and snow (Shokr and Sinha, 2015). The warm tail shows the presence of leads, but its peak is often too small (only visible in the log scale), and the different thin ice thicknesses in leads widen the lead temperature distribution. The more narrow distributions indicate the prevalence of thick, consolidated ice due to cold and calm conditions. For mid-winter flights, the distributions are wider for regional flights (**Figure 4C**) than for local flights (**Figure 4B**) because they include a larger variety of surface types due to the larger spatial extent. In the local flights, there is a transition from a wider distribution at the beginning of the winter season (blue) to a narrow distribution in mid-winter (yellow) and back to a wider distribution toward the end of the winter season (red). An indicator for the width of the distribution is the standard deviation of the surface temperature when the leads (warm tail) are excluded. The surface temperature standard deviation of the local flights decreased from 0.82 K on November 5, 2019, to 0.19 K on February 12, 2020, before it increased again to 1.03 K on April 21, 2020.

Table 1. Percentage value of lead area fraction from the local and regional scales, as presented in Figure 7

Date (year-month-day)	Local Fraction (%)	Regional Fraction (%)
2019-10-20	1.31	–[a]
2019-10-29	–	0.36
2019-11-05	0.06	–
2019-11-12	0.07	0.10
2019-11-19	1.73	–
2019-11-30	0.41	–
2019-12-06	–	0.86
2019-12-24	3.93	–
2019-12-25	3.56	–
2019-12-28	0.01	–
2019-12-30	–	0.56
2020-01-07	2.02	0.23
2020-01-16	0.00	1.37
2020-01-21	0.01	–
2020-01-23	–	1.66
2020-01-28	1.62	–
2020-02-04	2.68	–
2020-02-09	–	1.22
2020-02-12	0.37	–
2020-02-17	0.01	–
2020-02-27	0.01	–
2020-03-21	3.76	3.87
2020-04-23	1.42	–

[a]Not available.

We find substantial differences when comparing the mean surface temperature for the local and regional flights. In January 2020, there was a high density of flights, which allowed us to illustrate the variability between different scales (**Figure 4A**). On January 7 and 16, 2020, a local (black) and a regional (blue) flight were conducted on the same day, while the regional flight was about 3 h later in both cases (**Figure 4A**). Within the 3 h, the air temperature increased by 0.8 K on January 7 and decreased by 0.9 K on January 16. The average surface temperature increased by 0.5 K on January 7 and decreased by 3.0 K on January 16 for the regional flight. Thus, the trend is similar but, especially on January 16, the absolute change is larger. We assume the surface temperature was adjusting to the air temperature changes. One additional possible contribution is the change in lead area fraction (Section 4; **Table 1**). On January 7 the regional lead area fraction was much lower, close to zero, which

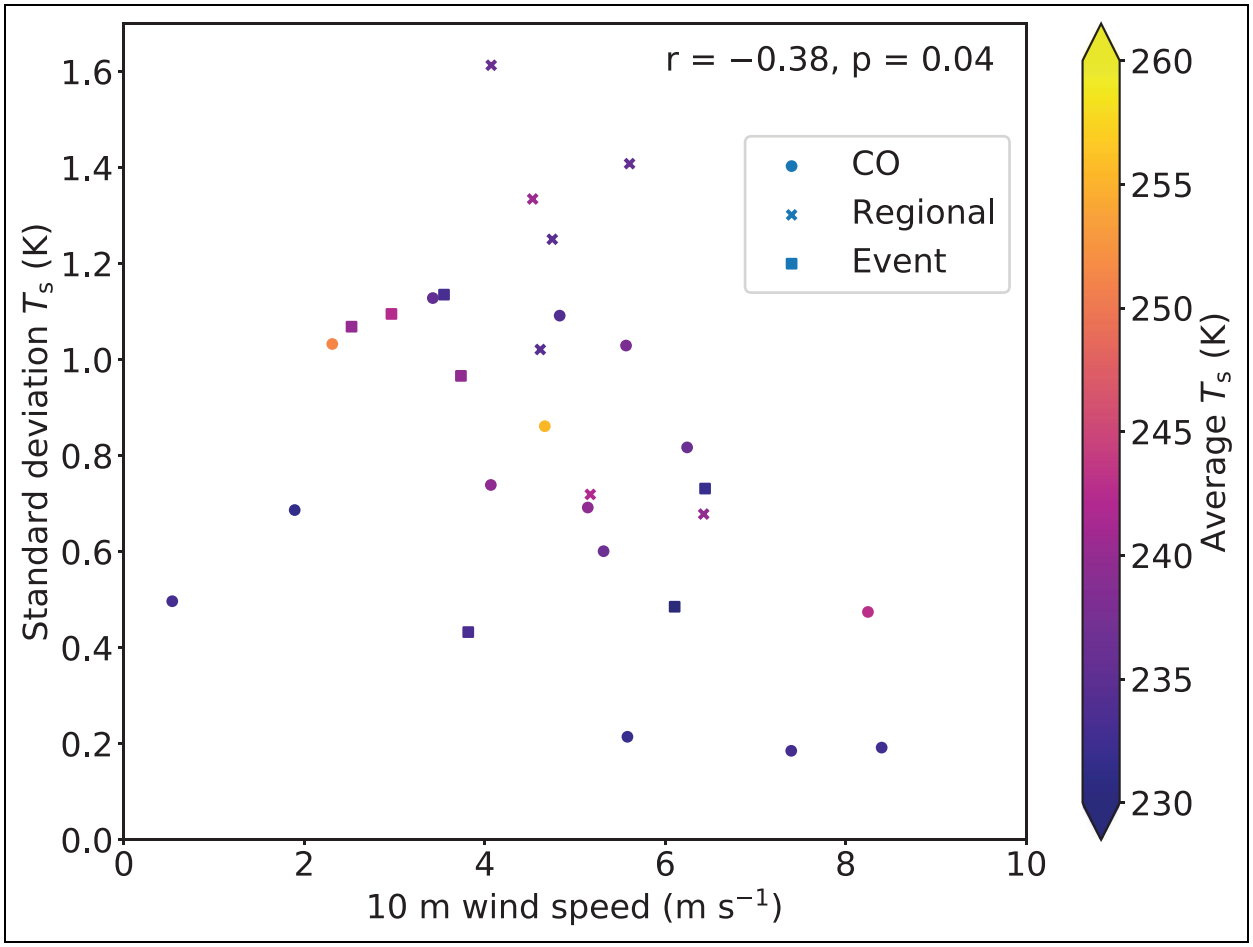

Figure 5. Connection between the standard deviation of surface temperature and the 10 m wind speed. For each flight, the standard deviation of the surface temperature is set in connection to the 10 m wind speed as the 10-min average around target time, shown as points. The correlation coefficient (r) is −0.38; the significance is 0.04 (p-value). The color of the points indicates the average surface temperature of the whole flight, as presented in the colorbar. The different point shapes represent the flight types: Central Observatory (CO, circle), L-Site/regional (cross), and events (square).

indicates a reduction in the average surface temperature compared to the local scale. On January 16, the decrease in the average surface temperature from the local to the regional flight contradicts the increased lead area fraction on the regional scale, while no leads were present on the local scale. Therefore, changes in ice types with different thermal properties, snowfall, or snow redistribution might have contributed to the changes in spatial surface temperature variability.

In the time series (**Figure 4A**), one can identify the close connection of the surface temperature to the atmospheric state, represented by the 2 m air temperature. Additionally, we considered the dependence of the surface temperature standard deviation as a measure of spatial variability on the 10 m wind speed (**Figure 5**). Here, leads were again excluded to have a comparable baseline of the thick ice. We expected a lower surface temperature standard deviation for higher wind speeds caused by an increased exchange between the surface and the atmosphere; indeed, a significant (p-value of 0.04) correlation of $r = -0.38$ exists between the surface temperature standard deviation and 10 m wind speed around the target time of the flight. This relationship with wind speed supports our assumptions that increasing wind speeds reduce surface temperature variability and can explain the greater sensible heat exchange due to faster air mass exchange. Because leads were not taken into account here, a potentially more dynamic ice pack that would result in more leads and, thus, higher temperatures can be ruled out. No correlation was found between the average surface temperatures and the standard deviation of the surface temperature. Although a low-temperature regime creates more compact and consolidated ice with uniform temperatures, even under cold conditions, deformation causes variability in ice classes with warmer surface temperatures, which increases the variation.

4. Winter lead area fraction

This section first presents an example of lead formation due to the November storm event that occurred during MOSAiC. The scale dependence of the evolution of the lead area fraction is then shown, as well as the connection between lead area fraction and the wind conditions.

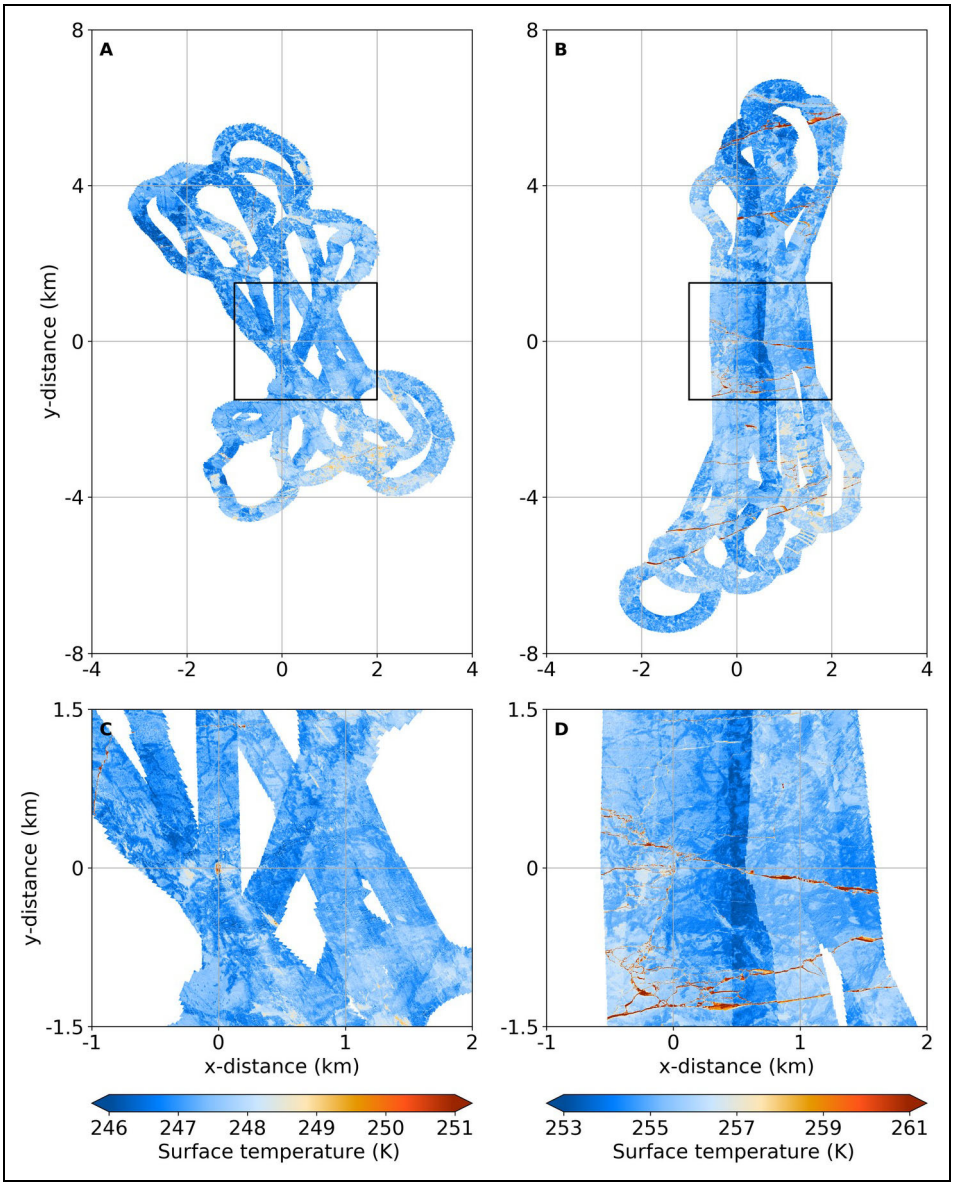

Figure 6. Surface temperature maps before and after the November storm event. Comparison of two time-fixed surface temperature maps displayed in relative coordinates (A and C) before the storm event on November 12, 2019, and (B and D) after the storm event on November 19, 2019, with their respective CO area around RV *Polarstern* (0,0). Note the different temperature ranges, adjusted to allow clearer visibility of the spatial variability of the temperature. For the flight on November 19, an increased area of warmer temperatures (reddish) is prominent.

4.1. Lead formation during the November storm event

Here, we discuss the storm event, which happened from November 16 to November 20, 2019 (Rinke et al., 2021). This event had a major influence on the MOSAiC Central Observatory due to several leads appearing across the measurement sites. It significantly influenced several measurements (Nicolaus et al., 2022; Shupe et al., 2022) including snow transport as discussed in Nandan et al. (2023). We conducted one flight before (November 12) and one flight after (November 19) the storm and compare both flights in **Figure 6**. This storm event with high wind speeds was associated with warm air advection. It resulted in the break-up of the sea ice along various fracture lines, which are visible in **Figure 6B** and **D**. The surface temperatures on November 19 after the storm were overall higher than before the storm event (mind the different temperature scales for **Figure 6A** and **C** versus **Figure 6B** and **D**). Before the storm, there were a few narrow cracks in the outer areas of the flight pattern (**Figure 6A**), but no prominent cracks in the vicinity of RV *Polarstern* (**Figure 6C**). The surface temperature map of November 19 includes warm linear structures throughout the CO area and beyond (**Figure 6B** and **D**), which caused an increase of lead area fraction from 0.07% (**Figure 6C**) to 1.73% (**Figure 6D**) and therewith to a higher surface temperature variability.

4.2. Scale dependence of the lead area fraction evolution

Here we discuss the spatio-temporal variability of the lead area fraction, which was calculated based on our lead

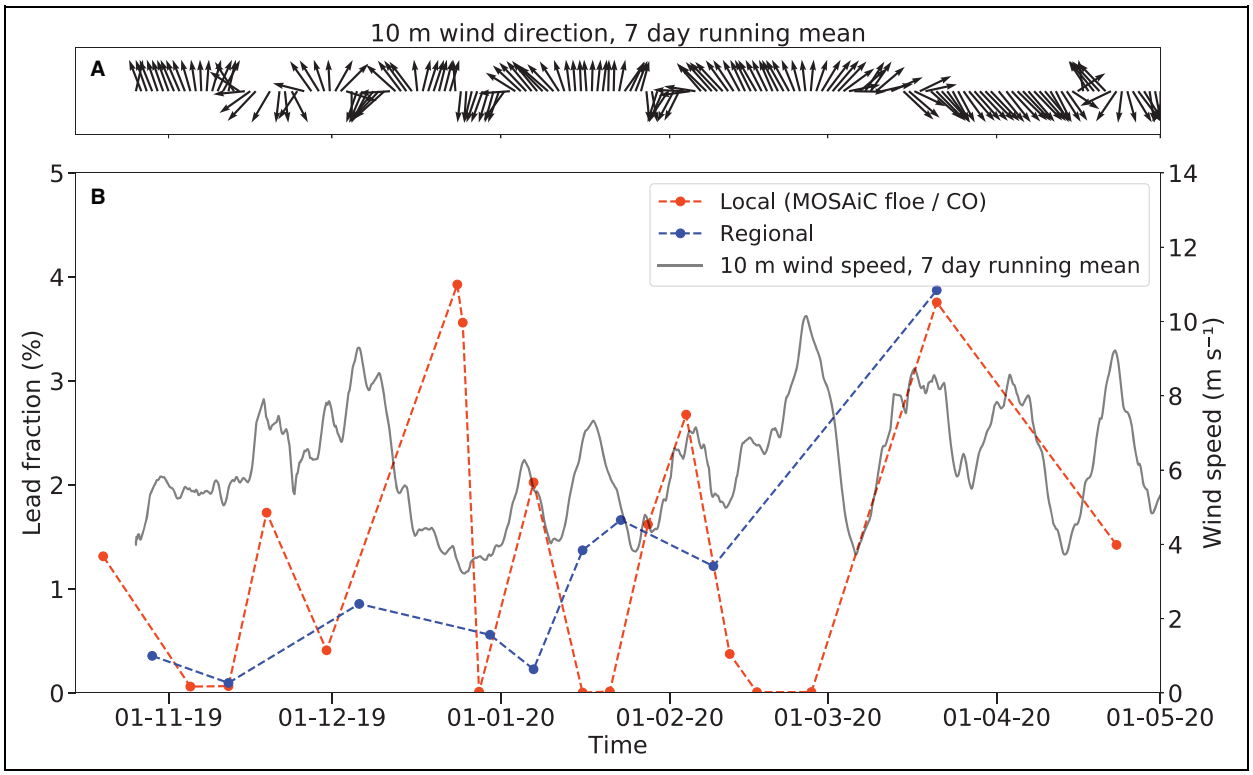

Figure 7. Evolution of the lead area fraction on different scales. (A) 10 m wind direction (North is up) as a 7-day running mean. (B) Temporal evolution of the lead area fraction throughout winter 2019/2020 from October 2, 2019, to April 23, 2020. The orange points show the lead area fraction for the Central Observatory (CO) area. The blue points illustrate the lead area fraction for the regional flights, visiting the L-Sites. The gray line shows the 10 m wind speed averaged to a 7-day running mean. Time is indicated as day-month-year. Note that there might have been a minor influence by in and out coming support vessels, which could have increased the lead area fraction by breaking the ice.

classification (Section 2.3). The local lead area fraction (orange line in **Figure 7**) is constrained to the CO area of 3 × 3 km (Figure S3 in the supplemental material). In the CO area, the same area around RV *Polarstern* was always covered, facilitating a better comparison of lead area fraction during the winter season than for the entire area covered by local flights. For the local flights, only the data in the CO area are considered. In most cases, the CO area lead area fraction is close to the one for the full local flights that are not constrained to the CO area (not shown). Only on October 20, 2019, is there a large difference in lead area fraction (1.3% for the CO area; 10.2% for the full local flight), because the majority of the detected leads were outside of the CO area. The data coverage of the CO area of more than 50% was achieved for all flights, and for the flights after November, the data coverage was higher at more than 75% (Figure S4 in the supplemental material).

The lead area fraction within the CO area shows high temporal variability between 0% and 4%, but no trend can be seen in the temporal evolution (**Figure 7**, orange line). For the November storm event (Section 4.1), the lead area fraction for the CO area increased from close to zero on November 12 to 1.7% on November 19. This lead area increase noticeably changed the heat exchange between ocean and atmosphere (Lüpkes et al., 2008).

For the regional scale, the lead area fraction was steady and low, between 0% and 1% until mid-January. Toward the end of the winter season on March 21, 2020, the lead area fraction increased to up to 4%. This increase in lead area fraction might be related to the increased number of storm events between January and April, compared to previous months (Section 3.1). Sea ice concentration and related lead area fraction strongly changed during and after passing of storms, in particular systems of several storms (Aue et al., 2023).

We can compare our results with other MOSAiC studies: e.g., Kortum et al. (2022) performed an ice classification based on synthetic aperture radar (SAR) satellite data during winter on the same scale (3 × 3 km) as our CO area. Our leads should be represented by the sum of open water and the young ice classes of their study, where daily data are available (higher temporal resolution than our data). Their daily data generally show a comparable magnitude to our lead area fraction below 5% in mid-winter but exceed this value on a few days by up to 15% around November 23, 2019. Additionally, during March and April, their lead area fraction is for a longer time on a higher level of up to 10%. The high values at the beginning of the winter in Kortum et al. (2022) might be caused by the characteristics of their method based on SAR data. The same method from Kortum et al. (2022) was applied on the regional scale with a 50 km radius (not shown). This regional lead area fraction peaked in mid-November at 6%, stayed below 4% and even lower during mid-winter,

and increased in the second half of March to 7% (Karl Kortum, personal communication, 08/12/2022). While we did not capture their peak in November and the absolute values differ by a few percentage points, the evolution of regional lead area from SAR data aligns well with our time series.

The evolution of regional lead area fraction also agrees well with another regional SAR-derived time series from Guo et al. (2022; scale of 71 × 71 km and 28 × 28 km). Their study shows a lead fraction range of 0–4% similar to ours, and their lead fraction also starts to increase in March.

The increase in lead area fraction observed in March in our data also aligns with the temporal evolution of lead area in Krumpen et al. (2021) based on MODIS satellite TIR data at a regional scale with a 10 km and 50 km radius. However, they observed a distinctly higher lead area fraction of up to 20%, derived from MODIS TIR satellite data. In summary, our results, derived for 3 km and 20–40 km scales, align reasonably well with the two SAR-based studies, despite the different temporal and spatial sampling, while for the MODIS TIR-based study the temporal evolution agrees but the absolute values differ.

Within our data, we observed scale-dependent differences in the lead area fraction, with less variability on the regional scale than on the local CO scale but no trend in the local scale, while the regional lead area fraction increased throughout the winter (**Figure 7**). Nevertheless, the overall magnitude was similar. Thus, the CO area is representative of the measurement sites in the CO of the MOSAiC expedition but the temporal development does not necessarily represent the lead area fraction on a larger scale. Nonetheless, the local data are helpful for a better understanding of the condition at and around the MOSAiC CO, particularly in connection to other in-situ measurements.

Our lead area fractions (0–4%) are comparable to other previous studies for different years and regions, with 1–2% reported by Marcq and Weiss (2012) and 2–3% reported by Lindsay and Rothrock (1995); both these winter lead area fractions were also derived in the central Arctic. Generally, the lead area fraction for the MOSAiC winter seems to align with the climatological mean, although it might have been influenced by the changing location due to the MOSAiC drift (Krumpen et al., 2021). Yet, comparing different lead area fraction retrievals remains challenging because of different definitions of leads, e.g., open leads versus leads covered by thin ice or even frost flowers, and the difference in methods used on different scales (von Albedyll et al., 2023).

4.3. Influence of atmospheric forcing

We are interested in the connection between lead area fraction and wind speed and wind direction, because wind events can cause increased ice movement and, therefore, possibly create more leads. Thus, we compared our lead area fraction to the 10 m wind speed and 10 m wind direction observations. We used the 7-day running mean to find prominent wind regimes rather than short-term fluctuations because we cannot represent these fluctuations with the limited temporal frequency of the helicopter flights.

Within the wind speed time series (**Figure 7B**), a few wind speed peaks are associated with changes in lead area fraction. Additionally, changes in the wind direction (**Figure 7A**), can introduce stress into sea ice that causes the ice to break up, resulting in an increased lead area faction. During our observation period, there were several wind direction changes within a short period of time. Our flights are only snapshots of a specific time with a weekly to biweekly frequency, while leads can open and close within hours; however, in most cases, they prevail for several days if not closed by another ice dynamic event. Eventually, the ice thickness and snow accumulation in leads becomes too thick to be discernible from the surrounding ice in TIR imagery.

Based on this knowledge, we suggest that high wind speed together with changes in wind direction can be the reason for an increase in the lead area fraction, as for the local scale during the November storm event (Section 4.1). Increases in wind speed alone are not the only reason causing changes in the lead area fraction. On the one hand, the highest local lead area fraction within the CO area of 4% at the end of December 2019 occurred after a regime of high wind speeds that lasted several days. During this increase in local lead area fraction the wind direction also changed, which might have caused a relaxation of the ice stress and an opening of leads even at lower wind speeds after the higher wind speed regime. On the other hand, during an increased wind speed regime in mid-January, when the regional lead area fraction increased, no leads were present on the local scale.

An additional atmospheric influence is the wind direction, particularly its changes. In December 2019, there were several strong changes in direction that potentially contributed to the increase in the lead area fraction since the beginning of December. Also, changes in wind direction could have caused changes in the lead area fraction at the end of December, as discussed above, and at the beginning of January 2020. As for the wind speed, we identify the wind direction as a contributing factor influencing lead area fraction.

The high variability in lead area fraction, especially for the local CO area, illustrates that local changes are limited in representing large-scale changes. Nevertheless, the local lead area fraction, when combined with other interdisciplinary measurements collected during MOSAiC, is useful for gaining a better understanding of physical processes like lead development or the influence of leads on the atmosphere or ocean.

5. Small-scale lead properties

In this section, we present results on the distribution of lead orientation and lead width for 1 m resolution data derived through lead segmentation (Section 2.4). Orientation and width may be critical parameters for evaluating the turbulent heat flux from leads (Tschudi et al., 2002). On the one hand, the efficiency of the heat transfer depends on the orientation relative to the wind direction (e.g., Tetzlaff et al., 2015). On the other hand, the heat

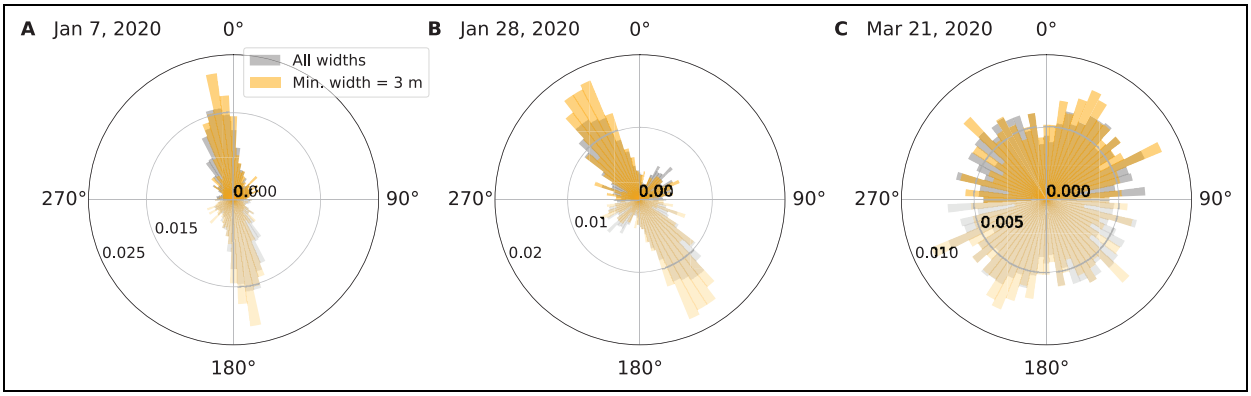

Figure 8. Orientation angles of leads for three example cases. Probability density distribution for the orientation angles of the flight from (A) January 7, 2020, (B) January 28, 2020, and (C) March 21, 2020, as polar histogram. The radius indicates the probability density, which is different for all three cases. Only lead segments with an axis ratio (major/minor) $\geq$2 are included. We discriminate between two cases: leads of all widths included (gray), and only leads with a minimum width of 3 m included (orange). The lead orientation has a range of only 180°, but is valid in both directions; they are mirrored to the opposite direction (slightly transparent). The total number of lead segments used for the histograms (270° to 90° only) for all width are (A) 1,736, (B) 1,326, and (C) 1,378; and for width $\geq$3 m are (A) 500, (B) 303, and (C) 464.

transfer is more efficient for narrow leads, which makes the transfer dependent on the lead width distribution (Marcq and Weiss, 2012).

5.1. Lead orientations

A good understanding of lead orientations is crucial because they represent the ice dynamics of the sea ice (Lindsay and Rothrock, 1995). Ringeisen et al. (2019) emphasized the lack of knowledge of lead orientation at the floe scale because of missing high resolution observations. Here, the MOSAiC observations contribute new data. Better knowledge of small-scale leads is also crucial for a good representation of ice rheology in sea ice models (Hutter et al., 2018; Ringeisen et al., 2021). The orientation of leads shows the effect of ice dynamics in sea ice, and is connected to prevailing regional wind and ocean currents (Lindsay and Rothrock, 1995). In the long term, leads have a non-random orientation during the Arctic winter, mainly influenced by coastlines and atmospheric and oceanic currents (e.g., Bröhan and Kaleschke, 2014). In general, the distribution of lead properties, including width and orientation, shows similarities across a wide range of scales between centimeters and kilometers (Schulson, 2004).

We analyzed lead orientations of nine local flights (full coverage, i.e., not restricted to the CO area), which in the CO area have a lead area fraction of $\geq$1%. This percentage ensures a sufficient presence of leads to perform a statistical analysis of lead orientations. We did not connect single lead segments (Section 2.4), which might have been parts of a single larger lead. This approach is sufficient for statistical lead width and lead orientation distribution analysis. Furthermore, we binned the lead orientations of each flight in 5° steps uniformly between −90° and 90°.

Comparing the nine flights between October 20, 2019, and April 23, 2020, we see a high temporal variability in the lead orientation distribution (see three examples in **Figure 8**), also shown for passive microwave-based analysis in Bröhan and Kaleschke (2014). We see a variation in the primary lead orientation throughout the winter but no prevailing orientations on longer time scales, potentially influenced by the changing location of the MOSAiC drift (see Text S2, Table S2, and Figure S5 in the supplemental material for more details).

There is a difference between using all data and the subset restricted to leads that are included in the power law, i.e., leads with >3 m width (see Section 5.2), but overall both approaches show the same picture (**Figure 8**). The variability of the lead orientations might depend on the regional wind patterns that create direction-related fracture patterns. An investigation of the reasons for the variability in lead orientation is beyond the scope of this study. Different to many previous studies is that that our data sets were collected far from land, which can introduce prevailing lead orientation by restricting ice drift in one direction, and that we were following the Lagrangian approach of the MOSAiC drift, which results in different locations of the Arctic Ocean being monitored.

5.2. Lead width

We discuss here the power law scaling of lead width (i.e., many more narrow leads than wide leads). Equation 1 gives the relation between lead width and number of observed leads (as probability density) of a respective width assuming a power law relationship:

$$f(x) = ax^{-b}. \quad (1)$$

The parameter a is the scaling parameter that is related to the number of measurements but is not further analyzed here. The parameter x is the variable lead width, and b is the power law exponent, determining the (negative) slope. Thus, a larger power law exponent b results in a steeper, i.e., more negative power law. The ratio of the classified segment area (shown in red in **Figure 3**) and the major axis length of the ellipse approximates the lead

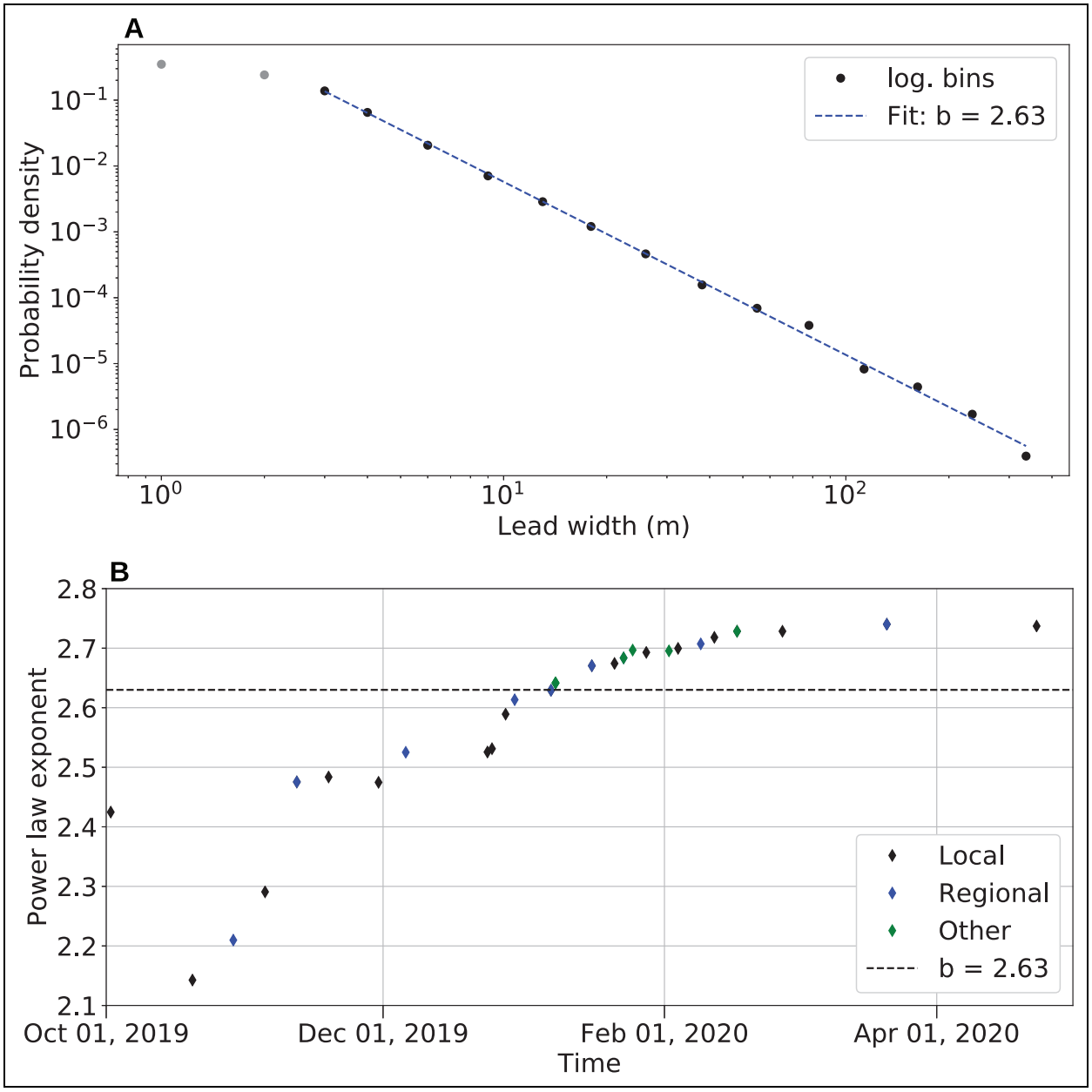

Figure 9. Lead width distribution with the power law fit for all and single flights. (A) The logarithmic frequencies of the lead widths of all 35 flights combined, and binned logarithmic, are represented as black points. The dashed blue line shows the negative power law fit exponent $b = 2.63$. The power law fit is constrained to the lead width ≥ 3 m. (B) Time series of the power law exponent for all 35 flights between October 2, 2019, and April 23, 2020, with black for local flights, blue for regional flights, and green for other flight types. The horizontal line marks the exponent of all flights (2.63) from panel A.

width. We detected in total 33,855 lead segments in our classified maps for all 35 flights. The number of segments should not be mistaken as the number of leads as smaller lead segments were not connected. The detected lead width varied between 1 m and 464 m.

For the distribution of the lead widths, we performed a linear fit with Equation 1 (**Figure 9A**) in the log-log space with logarithmic bins. We excluded leads smaller than 3 m width because they were too close to the spatial resolution of the data set to be fully resolved in the segmentation, as seen in the deviation from the power law below 3 m in **Figure 9**. This closeness is confirmed by the stabilization of the power law exponent for a minimum lead width of 3 m and larger (Figure S6 in the supplemental material). However, for a minimum lead width between 9 m and 26 m the power law exponent increases slightly. We do not know the reason for the increase but we hypothesize that the value is less reliable because of the strong decrease in number of lead segments that are available for the power law fit with increasing minimum lead width. Our power law is calculated up to the lead width of 336 m (largest logarithmic bin).

The resulting exponent of $b = 2.63$ agrees with literature values at the upper end of the previously found range

of exponent values (2.0 to 2.6; Wadhams, 1981; Wadhams et al., 1985; Marcq and Weiss, 2012; Wernecke and Kaleschke, 2015; Qu et al., 2019) and confirms the compatibility with other data sets. From the stability of b (Figure S6) we estimated the uncertainty of our b to be smaller than the range of the literature values of 2.0–2.6, as summarized in Muchow et al. (2021). Lindsay and Rothrock (1995) determined a smaller exponent of 1.6 ± 0.18 (less steep), which might differ because the power law is calculated to the lead width that is equal to the spatial resolution, and we see in our data that the power law is not valid close to the spatial resolution where the slope between the bins has a smaller absolute value.

In previous studies, the range of the power law exponent (dependent on the instrument and resolution) was determined starting between 20 m and 2 km lead widths (Muchow et al., 2021). Our study adds to the lower end of lead width, with a range down to 3 m, and shows that the power law agrees with other methods and resolutions. As expressed by the power law, there are many more leads with small lead width that were not resolved in previous studies. Also, our smallest resolvable lead width of 3 m is not likely the end of the lead width distribution. There were likely many cracks with a smaller width, which we did not resolve (but which can also be important for, e.g., heat flux estimates). Our exponent has the largest absolute value (i.e., most negative) compared to the literature values. The other studies were also based primarily on winter data (October–April) but were performed in different regions of the Arctic, which might have influenced the results due to different characteristics of the ice rheology. The power law distribution tells us that there are many more narrow leads than wider leads, which emphasizes the importance of small-scale features. The area contribution of the smallest leads were: 4% for lead width <3 m, which is below the minimum lead width of the power law; 64% for lead widths between 3 m and 100 m; and 32% for lead width >100 m.

Additionally, we found a seasonal dependence of the power law exponent, with a tendency of the exponent to increase throughout the winter season (**Figure 9B**). This seasonal increase in the power law exponent can also have a spatial component because of the drift into different regions during MOSAiC (**Figure 1**). The lowest absolute value of 2.14 for the power law exponent occurs at the start of the winter season in October (freeze-up time and consolidation of the ice north of the Laptev Sea), followed by a steady increase to 2.63 on January 7, 2020 (central Arctic). After another increase, the exponent then stabilizes at around 2.74 in March and April (North of Svalbard). We did not cover the melting and summer season, which again might introduce a change to the exponent. For the power law exponent, there is: no scale dependence, i.e., no variation between local and regional flight, nor on the same day (compare black and blue dots on **Figure 9B**); and no clear effect on the exponent by a rapid change in lead area fraction (Section 4.2) caused by, e.g., the November storm event between the flight on November 12 and November 19, 2019 (Section 4.1).

Lindsay and Rothrock (1995) presented the monthly average of the absolute value of the power law exponent for the central Arctic, with a decrease in the exponent from February to April, an increase between August and October, and another decrease from October to December. This pattern suggests a minimum power law exponent during summer, but there are no data for May, June, and July in Lindsay and Rothrock (1995). Our results present an opposite pattern to their findings, as we calculated an increase in the absolute value of the power law exponent between October and December and a stable exponent between February and April.

To provide possible explanations for why the power law exponent increases (relatively more narrow leads) throughout the winter in our case, we consider the following. Three exponents in October and at the beginning of November are low (2.1 to 2.3), probably because during the freeze-up phase the ice floes were still in free drift, which could cause relatively wider leads (a decrease in the exponent). The power law fit for these three flights deviates from the other flights. In December and January, the exponent increases from 2.5 to 2.7, which may be related to a more consolidated and thicker ice pack far away from the coastlines. These properties can be caused by a change in internal ice strength. This time period is also characterized by fewer storms and lower wind speeds (**Figure 7**). The stabilization at the end of the winter may be showing the maximum power law exponent that can be reached during winter before it decreases toward the melt season with free drift conditions (not included in our data set).

The clear power law relationship for the lead width found here supports the validity of our lead property data and that representative statistical conclusions can be obtained from it. Our results indicate that many leads in satellite remote sensing products with coarser spatial resolutions are not resolved. That many small leads are not resolved in satellite data could already be extrapolated from the power law found in previous studies, but is shown here for the first time down to a lead width of 3 m. Our widest leads are still narrower than the resolution of about 1 km of TIR satellites. Lead retrieval results vary (e.g., in frequency and how thick the ice in the lead can be) between different remote sensing approaches (von Albedyll et al., 2023). Thus, direct and absolute comparison of lead retrievals can be difficult for different products and resolutions. Nevertheless, the same physical principles (like the power law correspondence) are valid for different scales and resolutions (Wernecke and Kaleschke, 2015). We recommend that any lead width study should check and demonstrate that the power law scaling conditions have been fulfilled to increase confidence in the validity of the results obtained.

6. Discussion and conclusions

In this study we used high resolution surface temperature maps obtained from helicopter flights to examine small-scale lead properties along the MOSAiC drift during the winter season. On a local (5–10 km) and regional (20–40 km) scale, we investigated the variation in surface temperatures and the derived lead properties in time and space.

First, we investigated the surface temperatures and found: that its temporal variability was influenced by meteorological changes, such as warm air intrusions, often associated with high wind speeds; and that spatial variability over thick ice decreased as wind speed increased. Overall, the temporal evolution of the surface temperature followed the seasonal cycle of the 2 m air temperature. However, the results from the different flight patterns revealed scale-dependent differences in the spatial temperature variability. Understanding the surface temperature variability on a small scale in the central Arctic is crucial because of the lack of information on the meter scale. So far, TIR satellite data with a resolution of 1 km or coarser are the commonly used products in the Arctic.

Next, we retrieved classified lead maps for each flight based on a lead classification applied to the surface temperature maps using a dynamic temperature threshold. We observed scale-dependent differences for the derived lead area fraction as for the surface temperature variability. Here, the presence of leads with much higher surface temperatures compared to surrounding sea ice contributes to the spatial surface temperature variability. We see a high variability between 0% and 4%o of the local lead area fraction, e.g., the increase in lead area fraction during the November 2019 storm. On a regional scale, there was a more stable lead area fraction between 0% and 1% until January, followed by an increase to 4% in March. Temporal changes in lead area fraction were influenced by the wind conditions, i.e., speed and change of direction. This temporal lead area evolution agrees well with other MOSAiC studies on the local and regional scale.

Besides the lead area fraction, the properties of the single leads are crucial for sea ice processes on small scales. We investigated the lead width and orientation for all lead segments observed on each of the 35 flights. The three main findings are: (1) the lead width distribution followed a power law (Equation 1) with a negative exponent of $b = 2.63$ (narrow leads dominated over wide leads), which is consistent with previous research ($b =$ 1.6–2.6); (2) the power law exponent increased over the course of the winter; and (3) small-scale leads typically had one primary orientation. However, that orientation changed between the flights, throughout the winter season and with the changing location of the MOSAiC drift. Thus, no overall prevailing orientation was found. The abundance of small-scale leads emphasizes the need to better understand their physical processes, where our high spatial resolution data can help. These narrow leads are not included individually in the current TIR satellite data of about 1 km resolution (e.g., MODIS, which provides subfootprint lead fraction but no information on the distribution of lead width, e.g., if there is one large lead or several small leads).

Concluding, we find that the surface temperature maps are a valuable data set to investigate the spatial and temporal variability of the sea ice surface during winter. The strong temperature contrasts that we encountered during winter allowed us to classify leads and determine their properties, particularly their width and orientation. The following three key points highlight the main results of this study:

1. Winter surface temperatures showed a seasonal evolution with spatial scale-dependent variability (Section 3);
2. Lead fraction evolution differed on the local and regional scale, affected by the wind conditions, like the November storm (Section 4); and
3. Lead width distribution follows a power law with an exponent similar to literature values down to a lead width of 3 m (Section 5).

From this study, we identify a need for subgrid-scale parameterization of small-scale physical sea ice properties, like the lead width distribution, in satellite products and models. Meeting this need is essential for Arctic-climate investigations because the ocean–atmosphere heat exchange does not scale linearly with lead area fraction and is larger for narrower leads (Marcq and Weiss, 2012). Such investigations can help to improve the representation of small-scale processes of Arctic sea ice in winter. In a separate study (Thielke, 2023, Chapter 6), we perform a one-to-one comparison of the high resolution helicopter-borne data of this study with TIR satellite data, i.e., MODIS ice surface temperatures. The aim is to assess how well the impact of leads on the atmosphere is represented in the satellite retrieval. Additionally, comparisons with the deformation rate from buoy grids on different scales or intercomparison with helicopter-borne topography data could be used to better understand the characteristics of leads encountered during the MOSAiC expedition.

Data accessibility statement

- Helicopter-borne surface temperature maps, 1 m resolution: Thielke et al. (2022a)
- Lead classification maps, 1 m resolution: Thielke et al. (2022c)
- Atmospheric in-situ data: Cox et al. (2021) [updated version used]

Supplemental files

The supplemental files for this article can be found as follows:

Text S1 and S2; Tables S1 and S2; Figures S1–S6; attached as separate PDF file.

Acknowledgments and Funding

This work was supported by the German Ministry for Education and Research (BMBF) as part of the International Multidisciplinary drifting Observatory for the Study of the Arctic Climate (grant MOSAiC20192020). We acknowledge the funding by BMBF through the IceSense project (grant 03F0866B), by the Deutsche Forschungsgemeinschaft (DFG) through the International Research Training Group IRTG 1904 ArcTrain (grant 221211316), the MOSAiCmicrowaveRS project (grant 420499875), and the Transregional Collaborative Research Center TRR 172 (grant 268020496) “Arctic Amplification: Climate Relevant

Atmospheric and Surface Processes, and Feedback Mechanisms (AC)[3]." We thank all persons who contributed to the expedition of the Research Vessel *Polarstern* during MOSAiC in 2019–2020 (AWI_PS122_00) (Nixdorf et al., 2021), and especially HeliService and their pilots and technicians. Without them, the helicopter survey flights and the collection of the data would not have been possible. We thank Karl Kortum for providing the SAR sea ice type data and Janna Rückert for the discussions about this manuscript. We thank the two reviewers, guest editor, and editor for their helpful comments, which helped to improve the manuscript.

Competing interests

The authors have no competing interests, as defined by *Elementa*, that might be perceived to influence the research presented in this manuscript.

Author contributions

Contributed to conception and design: LT, GS, MH.

Contributed to acquisition of data: LT, GS, MH.

Contributed to analysis and interpretation of data: All authors.

Drafted the article: LT.

Revised the article: All authors.

Approved the submitted version for publication: All authors.

References

Alfred-Wegener-Institut Helmholtz-Zentrum für Polar- und Meeresforschung. 2017. Polar research and supply vessel POLARSTERN operated by the Alfred-Wegener-Institute. *Journal of Large-Scale Research Facilities* **3**: A119. DOI: http://dx.doi.org/10.17815/jlsrf-3-163.

Aue, L, **Röntgen, L**, **Dorn, W**, **Uotila, P**, **Vihma, T**, **Spreen, G**, **Rinke, A.** 2023. Impact of three intense winter cyclones on the sea ice cover in the Barents Sea: A case study with a coupled regional climate model. *Frontiers in Earth Science* **11**: 1112467. DOI: http://dx.doi.org/10.3389/feart.2023.1112467.

Bröhan, D, **Kaleschke, L.** 2014. A nine-year climatology of Arctic sea ice lead orientation and frequency from AMSR-E. *Remote Sensing* **6**(2): 1451–1475. DOI: http://dx.doi.org/10.3390/rs6021451.

Burger, W, **Burge, MJ.** 2009. Undergraduate topics in computer science, in Mackie, I, Abramsky, S, Hankin, C, Hinchey, M, Kozen, D, Nielson, HR, Skiena, SS, Stewart, I, Kizza, JM, Crole, R, Scott, E eds., *Principles of digital image processing: Core algorithms*. London, UK: Springer-Verlag: 1–332. DOI: http://dx.doi.org/10.1007/978-1-84800-195-4.

Cox, C, **Gallagher, M**, **Shupe, M**, **Persson, O**, **Solomon, A**, **Blomquist, B**, **Brooks, I**, **Costa, D**, **Gottas, D**, **Hutchings, J**, **Osborn, J**, **Morris, S**, **Preusser, A**, **Uttal, T**. 2021. 10-meter (m) meteorological flux tower measurements (Level 1 Raw), Multidisciplinary Drifting Observatory for the Study of Arctic Climate (MOSAiC), Central Arctic, October 2019–September 2020 [dataset]. Arctic Data Center. DOI: https://doi.org/10.18739/A2VM42Z5F.

Dai, A, **Luo, D**, **Song, M**, **Liu, J.** 2019. Arctic amplification is caused by sea-ice loss under increasing CO_2. *Nature Communications* **10**(1): 1–13. DOI: http://dx.doi.org/10.1038/s41467-018-07954-9.

Dethloff, K, **Maslowski, W**, **Hendricks, S**, **Lee, YJ**, **Goessling, HF**, **Krumpen, T**, **Haas, C**, **Handorf, D**, **Ricker, R**, **Bessonov, V**, **Cassano, JJ**, **Kinney, JC**, **Osinski, R**, **Rex, M**, **Rinke, A**, **Sokolova, J**, **Sommerfeld, A.** 2022. Arctic sea ice anomalies during the MOSAiC winter 2019/20. *The Cryosphere* **16**(3): 981–1005. DOI: http://dx.doi.org/10.5194/tc-16-981-2022.

Esau, IN. 2007. Amplification of turbulent exchange over wide Arctic leads: Large-eddy simulation study. *Journal of Geophysical Research: Atmospheres* **112**(D8): 225. DOI: http://dx.doi.org/10.1029/2006JD007225.

Fox-Kemper, B, **Hewitt, H**, **Xiao, C**, **Aalgeirsdóttir, G**, **Drijfhout, S**, **Edwards, T**, **Golledge, N**, **Hemer, M**, **Kopp, R**, **Krinner, G**, **Mix, A**, **Notz, D**, **Nowicki, S**, **Nurhati, I**, **Ruiz, L**, **Sallée, JB**, **Slangen, A**, **Yu, Y.** 2021. Ocean, cryosphere and sea level change, in Masson-Delmotte, V, Zhai, P, Pirani, A, Connors, S, Péan, C, Berger, S, Caud, N, Chen, Y, Goldfarb, L, Gomis, M, Huang, M, Leitzell, K, Lonnoy, E, Matthews, J, Maycock, T, Waterfield, T, Yelekçi, O, Yu, R, Zhou, B eds., *Climate change 2021: The physical science basis. Contribution of Working Group I to the sixth assessment report of the Intergovernmental Panel on Climate Change*. Cambridge, UK; New York, NY: Cambridge University Press: 1211–1362. DOI: http://dx.doi.org/10.1017/9781009157896.011.

Guo, W, **Itkin, P**, **Singha, S**, **Paul Doulgeris, A**, **Johansson, M**, **Spreen, G.** 2022. Sea ice classification of TerraSAR-X ScanSAR images for the MOSAiC expedition incorporating per-class incidence angle dependency of image texture. *The Cryosphere Discussions* **2022**: 1–29. DOI: http://dx.doi.org/10.5194/tc-2022-86.

Hutter, N, **Losch, M**, **Menemenlis, D.** 2018. Scaling properties of Arctic sea ice deformation in a high-resolution viscous-plastic sea ice model and in satellite observations. *Journal of Geophysical Research: Oceans* **123**(1): 672–687. DOI: http://dx.doi.org/10.1002/2017JC013119.

Intergovernmental Panel on Climate Change. 2021. *Climate change 2021: The physical science basis. Contribution of Working Group I to the sixth assessment report of the Intergovernmental Panel on Climate Change* [Masson-Delmotte, V, Zhai, P, Pirani, A, Connors, SL, Péan, C, Berger, S, Caud, N, Chen, Y, Goldfarb, L, Gomis, MI, Huang, M, Leitzell, K, Lonnoy, E, Matthews, JBR, Maycock, TK, Waterfield, T, Yelekçi, O, Yu, R, Zhou, B eds.]. Cambridge, UK; New York, NY: Cambridge University Press. DOI: http://dx.doi.org/10.1017/9781009157896.

Ivanova, N, **Rampal, P**, **Bouillon, S.** 2016. Error assessment of satellite-derived lead fraction in the Arctic.

The Cryosphere **10**(2): 585–595. DOI: http://dx.doi.org/10.5194/tc-10-585-2016.

Kortum, K, **Singha, S**, **Spreen, G.** 2022. Robust multiseasonal ice classification from high-resolution X-band SAR. *IEEE Transactions on Geoscience and Remote Sensing* **60**: 1–12. DOI: http://dx.doi.org/10.1109/TGRS.2022.3144731.

Krumpen, T, **Birrien, F**, **Kauker, F**, **Rackow, T**, **von Albedyll, L**, **Angelopoulos, M**, **Belter, HJ**, **Bessonov, V**, **Damm, E**, **Dethloff, K**, **Haapala, J**, **Haas, C**, **Harris, C**, **Hendricks, S**, **Hoelemann, J**, **Hoppmann, M**, **Kaleschke, L**, **Karcher, M**, **Kolabutin, N**, **Lei, R**, **Lenz, J**, **Morgenstern, A**, **Nicolaus, M**, **Nixdorf, U**, **Petrovsky, T**, **Rabe, B**, **Rabenstein, L**, **Rex, M**, **Ricker, R**, **Rohde, J**, **Shimanchuk, E**, **Singha, S**, **Smolyanitsky, V**, **Sokolov, V**, **Stanton, T**, **Timofeeva, A**, **Tsamados, M**, **Watkins, D.** 2020. The MOSAiC ice floe: Sediment-laden survivor from the Siberian shelf. *The Cryosphere* **14**(7): 2173–2187. DOI: http://dx.doi.org/10.5194/tc-14-2173-2020.

Krumpen, T, **von Albedyll, L**, **Goessling, HF**, **Hendricks, S**, **Juhls, B**, **Spreen, G**, **Willmes, S**, **Belter, HJ**, **Dethloff, K**, **Haas, C**, **Kaleschke, L**, **Katlein, C**, **Tian-Kunze, X**, **Ricker, R**, **Rostosky, P**, **Rückert, J**, **Singha, S**, **Sokolova, J.** 2021. MOSAiC drift expedition from October 2019 to July 2020: Sea ice conditions from space and comparison with previous years. *The Cryosphere* **15**(8): 3897–3920. DOI: http://dx.doi.org/10.5194/tc-15-3897-2021.

Kwok, R. 2018. Arctic sea ice thickness, volume, and multiyear ice coverage: Losses and coupled variability (1958–2018). *Environmental Research Letters* **13**(10). DOI: http://dx.doi.org/10.1088/1748-9326/aae3ec.

Kwok, R, **Spreen, G**, **Pang, S.** 2013. Arctic sea ice circulation and drift speed: Decadal trends and ocean currents. *Journal of Geophysical Research: Oceans* **118**(5): 2408–2425. DOI: http://dx.doi.org/10.1002/jgrc.20191.

Lindsay, R, **Rothrock, D.** 1995. Arctic sea ice leads from advanced very high resolution radiometer images. *Journal of Geophysical Research: Oceans* **100**(C3): 4533–4544. DOI: http://dx.doi.org/10.1029/94JC02393.

Lüpkes, C, **Vihma, T**, **Bimbaum, G**, **Wacker, U.** 2008. Influence of leads in sea ice on the temperature of the atmospheric boundary layer during polar night. *Geophysical Research Letters* **35**(3): 2–6. DOI: http://dx.doi.org/10.1029/2007GL032461.

Marcq, S, **Weiss, J.** 2012. Influence of sea ice lead-width distribution on turbulent heat transfer between the ocean and the atmosphere. *The Cryosphere* **6**(1): 143–156. DOI: http://dx.doi.org/10.5194/tc-6-143-2012.

Masuoka, E, **Fleig, A**, **Wolfe, R**, **Patt, F.** 1998. Key characteristics of MODIS data products. *IEEE Transactions on Geoscience and Remote Sensing* **36**(4): 1313–1323. DOI: http://dx.doi.org/10.1109/36.701081.

Maykut, GA. 1978. Energy exchange over young sea ice in the central Arctic. *Journal of Geophysical Research: Oceans* **83**(C7): 3646–3658. DOI: http://dx.doi.org/10.1029/JC083iC07p03646.

Maykut, GA. 1982. Large-scale heat exchange and ice production in the central Arctic. *Journal of Geophysical Research: Oceans* **87**(C10): 7971–7984. DOI: http://dx.doi.org/10.1029/JC087iC10p07971.

Meredith, M, **Sommerkorn, M**, **Cassotta, S**, **Derksen, C**, **Ekaykin, A**, **Hollowed, A**, **Kofinas, G**, **Mackintosh, A**, **Melbourne-Thomas, J**, **Muelbert, M**, **Ottersen, G**, **Pritchard, H**, **Schuur, E**. 2019. Polar regions, in Pörtner, HO, Roberts, D, MassonDelmotte, V, Zhai, P, Tignor, M, Poloczanska, E, Mintenbeck, K, Alegra, A, Nicolai, M, Okem, A, Petzold, J, Rama, B, Weyer, N eds., *IPCC special report on the ocean and cryosphere in a changing climate*. Cambridge, UK; New York, NY: Cambridge University Press: 203–320. DOI: http://dx.doi.org/10.1017/9781009157964.005.

Muchow, M, **Schmitt, AU**, **Kaleschke, L.** 2021. A lead-width distribution for Antarctic sea ice: A case study for the Weddell Sea with high-resolution Sentinel-2 images. *The Cryosphere* **15**(9): 4527–4537. DOI: http://dx.doi.org/10.5194/tc-15-4527-2021.

Najman, L, **Schmitt, M.** 1994. Watershed of a continuous function. *Signal Processing* **38**(1): 99–112. DOI: http://dx.doi.org/10.1016/0165-1684(94)90059-0.

Nandan, V, **Willatt, R**, **Mallett, R**, **Stroeve, J**, **Geldsetzer, T**, **Scharien, R**, **Tonboe, R**, **Yackel, J**, **Landy, J**, **Clemens-Sewall, D**, **Jutila, A**, **Wagner, DN**, **Krampe, D**, **Huntemann, M**, **Mahmud, M**, **Jensen, D**, **Newman, T**, **Hendricks, S**, **Spreen, G**, **Macfarlane, A**, **Schneebeli, M**, **Mead, J**, **Ricker, R**, **Gallagher, M**, **Duguay, C**, **Raphael, I**, **Polashenski, C**, **Tsamados, M**, **Matero, I**, **Hoppmann, M.** 2023. Wind redistribution of snow impacts the Ka- and Ku-band radar signatures of Arctic sea ice. *The Cryosphere* **17**(6): 2211–2229. DOI: http://dx.doi.org/10.5194/tc-17-2211-2023.

Nicolaus, M, **Perovich, DK**, **Spreen, G**, **Granskog, MA**, **von Albedyll, L**, **Angelopoulos, M**, **Anhaus, P**, **Arndt, S**, **Belter, HJ**, **Bessonov, V**, **Birnbaum, G**, **Brauchle, J**, **Calmer, R**, **Cardellach, E**, **Cheng, B**, **Clemens-Sewall, D**, **Dadic, R**, **Damm, E**, **de Boer, G**, **Demir, O**, **Dethloff, K**, **Divine, DV**, **Fong, AA**, **Fons, S**, **Frey, MM**, **Fuchs, N**, **Gabarró, C**, **Gerland, S**, **Goessling, HF**, **Gradinger, R**, **Haapala, J**, **Haas, C**, **Hamilton, J**, **Hannula, HR**, **Hendricks, S**, **Herber, A**, **Heuzé, C**, **Hoppmann, M**, **Høyland, KV**, **Huntemann, M**, **Hutchings, JK**, **Hwang, B**, **Itkin, P**, **Jacobi, HW**, **Jaggi, M**, **Jutila, A**, **Kaleschke, L**, **Katlein, C**, **Kolabutin, N**, **Krampe, D**, **Kristensen, SS**, **Krumpen, T**, **Kurtz, N**, **Lampert, A**, **Lange, BA**, **Lei, R**, **Light, B**, **Linhardt, F**, **Liston, GE**, **Loose, B**, **Macfarlane, AR**, **Mahmud, M**, **Matero, IO**, **Maus, S**, **Morgenstern, A**, **Naderpour, R**, **Nandan, V**, **Niubom, A**, **Oggier, M**, **Oppelt, N**, **Pätzold, F**, **Perron, C**, **Petrovsky, T**, **Pirazzini, R**, **Polashenski, C**, **Rabe, B**, **Raphael, IA**, **Regnery, J**, **Rex, M**, **Ricker, R**,

Riemann-Campe, K, **Rinke, A**, **Rohde, J**, **Salganik, E**, **Scharien, RK**, **Schiller, M**, **Schneebeli, M**, **Semmling, M**, **Shimanchuk, E**, **Shupe, MD**, **Smith, MM**, **Smolyanitsky, V**, **Sokolov, V**, **Stanton, T**, **Stroeve, J**, **Thielke, L**, **Timofeeva, A**, **Tonboe, RT**, **Tavri, A**, **Tsamados, M**, **Wagner, DN**, **Watkins, D**, **Webster, M**, **Wendisch, M**. 2022. Overview of the MOSAiC expedition: Snow and sea ice. *Elementa: Science of the Anthropocene* **10**(1). DOI: http://dx.doi.org/10.1525/elementa.2021.000046.

Nixdorf, U, **Dethloff, K**, **Rex, M**, **Shupe, M**, **Sommerfeld, A**, **Perovich, DK**, **Nicolaus, M**, **Heuzé, C**, **Rabe, B**, **Loose, B**, **Damm, E**, **Gradinger, R**, **Fong, A**, **Maslowski, W**, **Rinke, A**, **Kwok, R**, **Spreen, G**, **Wendisch, M**, **Herber, A**, **Hirsekorn, M**, **Mohaupt, V**, **Frickenhaus, S**, **Immerz, A**, **Weiss-Tuider, K**, **König, B**, **Mengedoht, D**, **Regnery, J**, **Gerchow, P**, **Ransby, D**, **Krumpen, T**, **Morgenstern, A**, **Haas, C**, **Kanzow, T**, **Rack, FR**, **Saitzev, V**, **Sokolov, V**, **Makarov, A**, **Schwarze, S**, **Wunderlich, T**, **Wurr, K**, **Boetius, A.** 2021. MOSAiC extended acknowledgement. Zenodo. DOI: http://dx.doi.org/10.5281/zenodo.5541624.

Qu, M, **Pang, X**, **Zhao, X**, **Zhang, J**, **Ji, Q**, **Fan, P.** 2019. Estimation of turbulent heat flux over leads using satellite thermal images. *The Cryosphere* **13**(6): 1565–1582. DOI: http://dx.doi.org/10.5194/tc-13-1565-2019.

Rabe, B, **Heuzé, C**, **Regnery, J**, **Aksenov, Y**, **Allerholt, J**, **Athanase, M**, **Bai, Y**, **Basque, C**, **Bauch, D**, **Baumann, TM**, **Chen, D**, **Cole, ST**, **Craw, L**, **Davies, A**, **Damm, E**, **Dethloff, K**, **Divine, DV**, **Doglioni, F**, **Ebert, F**, **Fang, YC**, **Fer, I**, **Fong, AA**, **Gradinger, R**, **Granskog, MA**, **Graupner, R**, **Haas, C**, **He, H**, **He, Y**, **Hoppmann, M**, **Janout, M**, **Kadko, D**, **Kanzow, T**, **Karam, S**, **Kawaguchi, Y**, **Koenig, Z**, **Kong, B**, **Krishfield, RA**, **Krumpen, T**, **Kuhlmey, D**, **Kuznetsov, I**, **Lan, M**, **Laukert, G**, **Lei, R**, **Li, T**, **Torres-Valdés, S**, **Lin, L**, **Lin, L**, **Liu, H**, **Liu, N**, **Loose, B**, **Ma, X**, **McKay, R**, **Mallet, M**, **Mallett, RDC**, **Maslowski, W**, **Mertens, C**, **Mohrholz, V**, **Muilwijk, M**, **Nicolaus, M**, **O'Brien, JK**, **Perovich, D**, **Ren, J**, **Rex, M**, **Ribeiro, N**, **Rinke, A**, **Schaffer, J**, **Schuffenhauer, I**, **Schulz, K**, **Shupe, MD**, **Shaw, W**, **Sokolov, V**, **Sommerfeld, A**, **Spreen, G**, **Stanton, T**, **Stephens, M**, **Su, J**, **Sukhikh, N**, **Sundfjord, A**, **Thomisch, K**, **Tippenhauer, S**, **Toole, JM**, **Vredenborg, M**, **Walter, M**, **Wang, H**, **Wang, L**, **Wang, Y**, **Wendisch, M**, **Zhao, J**, **Zhou, M**, **Zhu, J**. 2022. Overview of the MOSAiC expedition: Physical oceanography. *Elementa: Science of the Anthropocene* **10**(1). DOI: http://dx.doi.org/10.1525/elementa.2021.00062.

Rampal, P, **Weiss, J**, **Marsan, D.** 2009. Positive trend in the mean speed and deformation rate of Arctic sea ice, 1979–2007. *Journal of Geophysical Research: Oceans* **114**(5). DOI: http://dx.doi.org/10.1029/2008JC005066.

Ridler, TW, **Calvard, S.** 1978. Picture thresholding using an iterative selection method. *IEEE Transactions on Systems, Man, and Cybernetics* **8**(8): 630–632. DOI: http://dx.doi.org/10.1109/TSMC.1978.4310039.

Ringeisen, D, **Losch, M**, **Bruno Tremblay, L**, **Hutter, N.** 2019. Simulating intersection angles between conjugate faults in sea ice with different viscous-plastic rheologies. *The Cryosphere* **13**(4): 1167–1186. DOI: http://dx.doi.org/10.5194/tc-13-1167-2019.

Ringeisen, D, **Tremblay, LB**, **Losch, M.** 2021. Non-normal flow rules affect fracture angles in sea ice viscous-plastic rheologies. *The Cryosphere* **15**(6): 2873–2888. DOI: http://dx.doi.org/10.5194/tc-15-2873-2021.

Rinke, A, **Cassano, JJ**, **Cassano, EN**, **Jaiser, R**, **Handorf, D.** 2021. Meteorological conditions during the MOSAiC expedition. *Elementa: Science of the Anthropocene* **9**(1): 0023. DOI: http://dx.doi.org/10.1525/elementa.2021.00023.

Schulson, EM. 2004. Compressive shear faults within Arctic sea ice: Fracture on scales large and small. *Journal of Geophysical Research: Oceans* **109**(7). DOI: http://dx.doi.org/10.1029/2003JC002108.

Serreze, MC, **Barrett, AP**, **Stroeve, JC**, **Kindig, DN**, **Holland, MM.** 2009. The emergence of surface-based Arctic amplification. *The Cryosphere* **3**(1): 11–19. DOI: http://dx.doi.org/10.5194/tc-3-11-2009.

Serreze, MC, **Barry, RG.** 2011. Processes and impacts of Arctic amplification: A research synthesis. *Global and Planetary Change* **77**(1): 85–96. DOI: http://dx.doi.org/10.1016/j.gloplacha.2011.03.004.

Shokr, M, **Sinha, N**. 2015. *Sea ice: Physics and remote sensing*. Hoboken, NJ: John Wiley & Sons.

Shupe, MD, **Rex, M**, **Blomquist, B**, **Persson, POG**, **Schmale, J**, **Uttal, T**, **Althausen, D**, **Angot, H**, **Archer, S**, **Bariteau, L**, **Beck, I**, **Bilberry, J**, **Bucci, S**, **Buck, C**, **Boyer, M**, **Brasseur, Z**, **Brooks, IM**, **Calmer, R**, **Cassano, J**, **Castro, V**, **Chu, D**, **Costa, D**, **Cox, CJ**, **Creamean, J**, **Crewell, S**, **Dahlke, S**, **Damm, E**, **de Boer, G**, **Deckelmann, H**, **Dethloff, K**, **Dütsch, M**, **Ebell, K**, **Ehrlich, A**, **Ellis, J**, **Engelmann, R**, **Fong, AA**, **Frey, MM**, **Gallagher, MR**, **Ganzeveld, L**, **Gradinger, R**, **Graeser, J**, **Greenamyer, V**, **Griesche, H**, **Griffiths, S**, **Hamilton, J**, **Heinemann, G**, **Helmig, D**, **Herber, A**, **Heuzé, C**, **Hofer, J**, **Houchens, T**, **Howard, D**, **Inoue, J**, **Jacobi, HW**, **Jaiser, R**, **Jokinen, T**, **Jourdan, O**, **Jozef, G**, **King, W**, **Kirchgaessner, A**, **Klingebiel, M**, **Krassovski, M**, **Krumpen, T**, **Lampert, A**, **Landing, W**, **Laurila, T**, **Lawrence, D**, **Lonardi, M**, **Loose, B**, **Lüpkes, C**, **Maahn, M**, **Macke, A**, **Maslowski, W**, **Marsay, C**, **Maturilli, M**, **Mech, M**, **Morris, S**, **Moser, M**, **Nicolaus, M**, **Ortega, P**, **Osborn, J**, **Pätzold, F**, **Perovich, DK**, **Petäjä, T**, **Pilz, C**, **Pirazzini, R**, **Posman, K**, **Powers, H**, **Pratt, KA**, **Preußer, A**, **Quéléver, L**, **Radenz, M**, **Rabe, B**, **Rinke, A**, **Sachs, T**, **Schulz, A**, **Siebert, H**, **Silva, T**, **Solomon, A**, **Sommerfeld, A**, **Spreen, G**, **Stephens, M**, **Stohl, A**, **Svensson, G**, **Uin, J**, **Viegas, J**, **Voigt, C**, **von der Gathen, P**, **Wehner, B**, **Welker, JM**, **Wendisch, M**, **Werner, M**, **Xie, Z**, **Yue, F**. 2022. Overview of the MOSAiC expedition: Atmosphere.

Elementa: Science of the Anthropocene **10**(1): 00060. DOI: http://dx.doi.org/10.1525/elementa.2021.00060.

Shupe, MD, **Rex, M**, **Dethloff, K**, **Damm, E**, **Fong, AA**, **Gradinger, R**, **Heuzé, C**, **Loose, B**, **Makarov, A**, **Maslowski, W**, **Nicolaus, M**, **Perovich, D**, **Rabe, B**, **Rinke, A**, **Sokolov, V**, **Sommerfeld, A**. 2020. Arctic report card 2020: The MOSAiC expedition: A year drifting with the Arctic sea ice. NOAA. DOI: http://dx.doi.org/10.25923/9g3v-xh92.

Spreen, G, **Kern, S.** 2017. Methods of satellite remote sensing of sea ice, in Thomas, DN ed., *Sea ice*. Chichester, UK: John Wiley & Sons: 239–260.

Spreen, G, **Kwok, R**, **Menemenlis, D.** 2011. Trends in Arctic sea ice drift and role of wind forcing: 1992–2009. *Geophysical Research Letters* **38**(19): 1–6. DOI: http://dx.doi.org/10.1029/2011GL048970.

Tetzlaff, A, **Lüpkes, C**, **Hartmann, J.** 2015. Aircraft-based observations of atmospheric boundary-layer modification over Arctic leads. *Quarterly Journal of the Royal Meteorological Society* **141**(692): 2839–2856. DOI: http://dx.doi.org/10.1002/qj.2568.

Thielke, L. 2023. Winter sea ice characteristics in the central Arctic from thermal infrared imaging [PhD thesis]. Bremen, Germany: University of Bremen. DOI: http://dx.doi.org/10.26092/elib/2305.

Thielke, L, **Huntemann, M**, **Hendricks, S**, **Jutila, A**, **Ricker, R**, **Spreen, G.** 2022a. Helicopter-borne thermal infrared sea ice surface temperature maps with 1 m resolution during the MOSAiC expedition, NetCDF format, version 3 [dataset]. PANGAEA. DOI: https://doi.org/10.1594/PANGAEA.950683.

Thielke, L, **Huntemann, M**, **Hendricks, S**, **Jutila, A**, **Ricker, R**, **Spreen, G.** 2022b. Sea ice surface temperatures from helicopter-borne thermal infrared imaging during the MOSAiC expedition. *Scientific Data* **9**(1): 1–16. DOI: http://dx.doi.org/10.1038/s41597-022-01461-9.

Thielke, L, **Huntemann, M**, **Spreen, G**. 2022c. Lead classification maps from helicopter-borne surface temperatures with 1 m resolution during the MOSAiC expedition [dataset]. PANGAEA. DOI: https://doi.org/10.1594/PANGAEA.951568.

Tschudi, MA, **Curry, JA**, **Maslanik, JA.** 2002. Characterization of springtime leads in the Beaufort/Chukchi seas from airborne and satellite observations during FIRE/SHEBA. *Journal of Geophysical Research: Oceans* **107**(C10): 1–14. DOI: http://dx.doi.org/10.1029/2000jc000541.

Vihma, T, **Pirazzini, R.** 2005. On the factors controlling the snow surface and 2-m air temperatures over the Arctic sea ice in winter. *Boundary-Layer Meteorology* **117**(1): 73–90. DOI: http://dx.doi.org/10.1007/s10546-004-5938-7.

Vihma, T, **Pirazzini, R**, **Fer, I**, **Renfrew, IA**, **Sedlar, J**, **Tjernström, M**, **Lüpkes, C**, **Nygård, T**, **Notz, D**, **Weiss, J**, **Marsan, D**, **Cheng, B**, **Birnbaum, G**, **Gerland, S**, **Chechin, D**, **Gascard, JC.** 2014. Advances in understanding and parameterization of small-scale physical processes in the marine Arctic climate system: A review. *Atmospheric Chemistry and Physics* **14**(17): 9403–9450. DOI: http://dx.doi.org/10.5194/acp-14-9403-2014.

von Albedyll, L, **Hendricks, S**, **Hutter, N**, **Murashkin, D**, **Kaleschke, L**, **Willmes, S**, **Thielke, L**, **Tian-Kunze, X**, **Spreen, G**, **Haas, C.** 2023. Lead fractions from SAR-derived sea ice divergence during MOSAiC. *The Cryosphere Discussions* **2023**: 1–39. DOI: http://dx.doi.org/10.5194/tc-2023-123.

Wadhams, P. 1981. Sea-ice topography of the Arctic Ocean in the region 70 W to 25 E. *Philosophical Transactions of the Royal Society of London Series A, Mathematical and Physical Sciences* **302**(1464): 45–85. DOI: http://dx.doi.org/10.1098/rsta.1981.0157.

Wadhams, P, **McLaren, AS**, **Weintraub, R.** 1985. Ice thickness distribution in Davis Strait in February from submarine sonar profiles. *Journal of Geophysical Research: Oceans* **90**(C1): 1069–1077. DOI: http://dx.doi.org/10.1029/JC090iC01p01069.

Wang, Q, **Danilov, S**, **Jung, T**, **Kaleschke, L**, **Wernecke, A.** 2016. Sea ice leads in the Arctic Ocean: Model assessment, interannual variability and trends. *Geophysical Research Letters* **43**(13): 7019–7027. DOI: http://dx.doi.org/10.1002/2016GL068696.

Wang, S, **Wang, Q**, **Jordan, RE**, **Persson, PO.** 2001. Interactions among longwave radiation of clouds, turbulence, and snow surface temperature in the Arctic: A model sensitivity study. *Journal of Geophysical Research: Atmospheres* **106**(D14): 15323–15333. DOI: http://dx.doi.org/10.1029/2000JD900358.

Wendisch, M, **Brückner, M**, **Burrows, JP**, **Crewell, S**, **Dethloff, K**, **Ebell, K**, **Lüpkes, C**, **Macke, A**, **Notholt, J**, **Quaas, J**, **Rinke, A**, **Tegen, I.** 2017. Understanding causes and effects of rapid warming in the Arctic. *Eos* **98**. DOI: http://dx.doi.org/10.1029/2017EO064803.

Wernecke, A, **Kaleschke, L.** 2015. Lead detection in Arctic sea ice from CryoSat-2: Quality assessment, lead area fraction and width distribution. *The Cryosphere* **9**(5): 1955–1968. DOI: http://dx.doi.org/10.5194/tc-9-1955-2015.

Willmes, S, **Heinemann, G.** 2015. Pan-Arctic lead detection from MODIS thermal infrared imagery. *Annals of Glaciology* **56**(69): 29–37. DOI: http://dx.doi.org/10.3189/2015AoG69A615.

Willmes, S, **Heinemann, G.** 2016. Sea-ice wintertime lead frequencies and regional characteristics in the Arctic, 2003–2015. *Remote Sensing* **8**(1): 4. DOI: http://dx.doi.org/10.3390/rs8010004.

World Meteorological Organization. 2014. Sea ice nomenclature. World Meteorological Organization. Available at https://library.wmo.int/idurl/4/41953. Accessed March 19, 2024.

Yu, Y, **Rothrock, DA.** 1996. Thin ice thickness from satellite thermal imagery. *Journal of Geophysical Research : Oceans* **101**(C11): 25753–25766. DOI: http://dx.doi.org/10.1029/96JC02242.

How to cite this article: Thielke, L, Spreen, G, Huntemann, M, Murashkin, D. 2024. Spatio-temporal variability of small-scale leads based on helicopter maps of winter sea ice surface temperatures. *Elementa: Science of the Anthropocene* 12(1). DOI: https://doi.org/10.1525/elementa.2023.00023

Domain Editor-in-Chief: Jody W. Deming, University of Washington, Seattle, WA, USA

Guest Editor: Marcel Nicolaus, Alfred-Wegener-Institut Helmholtz-Zentrum für Polar- und Meeresforschung, Bremerhaven, Germany

Knowledge Domain: Ocean Science

Part of an Elementa Special Feature: The Multidisciplinary Drifting Observatory for the Study of Arctic Climate (MOSAiC)

Published: March 27, 2024 **Accepted:** December 24, 2023 **Submitted:** January 27, 2023

ELEMENTA Science of the Anthropocene

Elem Sci Anth is a peer-reviewed open access journal published by University of California Press.

OPEN ACCESS